

## Positrons from dark matter annihilation in the galactic halo: theoretical uncertainties

T. Delahaye,<sup>1,\*</sup> R. Lineros,<sup>2,†</sup> F. Donato,<sup>2,‡</sup> N. Fornengo,<sup>2,§</sup> and P. Salati<sup>1,¶</sup><sup>1</sup>*Laboratoire d'Annecy-le-Vieux de Physique Théorique LAPTH, CNRS-SPM  
and Université de Savoie 9, Chemin de Bellevue, B.P.110 74941 Annecy-le-Vieux, France*<sup>2</sup>*Dipartimento di Fisica Teorica, Università di Torino  
and Istituto Nazionale di Fisica Nucleare, via P. Giuria 1, I-10125 Torino, Italy*

(Dated: November 7, 2018)

Indirect detection signals from dark matter annihilation are studied in the positron channel. We discuss in detail the positron propagation inside the galactic medium: we present novel solutions of the diffusion and propagation equations and we focus on the determination of the astrophysical uncertainties which affect the positron dark matter signal. We find dark matter scenarios and propagation models that nicely fit existing data on the positron fraction. Finally, we present predictions both on the positron fraction and on the flux for already running or planned space experiments, concluding that they have the potential to discriminate a possible signal from the background and, in some cases, to distinguish among different astrophysical propagation models.

PACS numbers: 95.35.+d,98.35.Gi,11.30.Pb,95.30.Cq

## I. INTRODUCTION

The quest for the identification of dark matter (DM), together with the comprehension of the nature of dark energy, is one of the most challenging problems in the understanding of the physical world. It is therefore of utmost importance to address the problem of the detection of the astronomical DM with different techniques and in different channels: in underground laboratories, in neutrino telescopes, in large-area surface detectors as well as in space. Many efforts in both direct and indirect DM detection have been done in the last decade, and major breakthroughs are expected in the following years from the underground facilities and antimatter searches in space. In the same period, the LHC will provide crucial information on possible extensions of the Standard Model of particle physics, where the most viable DM candidates are predicted. We therefore are faced with the quest of signal predictions as detailed as possible, accompanied by a realistic estimation of their uncertainties.

This paper deals with the indirect detection of DM through positrons from the DM pair annihilation inside the galactic halo. Secondary positrons and electrons are produced in the Galaxy from the collisions of cosmic-ray proton and helium nuclei on the interstellar medium [1] and are an important tool for the comprehension of cosmic-ray propagation. Data on the cosmic positron flux

(often reported in terms of the positron fraction) have been collected by several experiments [2, 3, 4, 5, 6, 7]. In particular, the HEAT data [2] mildly indicate a possible excess of the positron fraction (see Eq. 32) for energies above 10 GeV and with respect to the available calculations for the secondary component [1]. Different astrophysical contributions to the positron fraction in the 10 GeV region have been explored [2], but only more accurate and energy extended data could shed light on the effective presence of a bump in the positron fraction and on its physical interpretation. Alternatively, it has been conjectured that the possible excess of positrons found in the HEAT data could be due to the presence of DM annihilation in the galactic halo [8, 9]. This interpretation, though very exciting, is at some point limited by the uncertainties in the halo structure and in the cosmic ray propagation modeling. Recently, it has been shown that the boost factor due to substructures in the DM halo depends on the positron energy and on the statistical properties of the DM distribution [10]. In addition, it has been pointed out that its numerical values is quite modest [11].

The present work is about the issue of the propagation of primary positrons. We inspect the full solution of the diffusion equation in a two-zone model already tested on several stable and radioactive species [12] and quantify the uncertainties due to propagation models, in connection with the positron production modes. Our results will be applied to experiments such as PAMELA and AMS-02, which are expected to bring a breakthrough in the cosmic antimatter searches and in the understanding of the positron component. In Sect. II we present the solutions to the diffusion equation with both the Green function formalism and the Bessel method, with a source

\*Electronic address: [delahaye@lapp.in2p3.fr](mailto:delahaye@lapp.in2p3.fr)†Electronic address: [lineros@to.infn.it](mailto:lineros@to.infn.it)‡Electronic address: [donato@to.infn.it](mailto:donato@to.infn.it)§Electronic address: [fornengo@to.infn.it](mailto:fornengo@to.infn.it)¶Electronic address: [salati@lapp.in2p3.fr](mailto:salati@lapp.in2p3.fr)

term due to the pair annihilations of DM particles. We introduce the diffusive halo function, the integral on the diffusive zone encoding the information relevant to cosmic ray propagation through its fundamental parameters. In Sect. III we evaluate the uncertainties due to propagation models on the diffusive halo function, discussing the physical properties of the propagation parameter configurations giving the extremes of the uncertainty bands. The positron fluxes and the relevant positron fraction are presented in Sect. IV, where we compare our results to existing data and elaborate predictions for present running or planned experiments in space. In Sect. V we draw our conclusions.

## II. THE DIFFUSION EQUATION AND ITS SOLUTIONS

The propagation of positrons in the galactic medium is governed by the transport equation

$$\frac{\partial \psi}{\partial t} - \nabla \cdot \{K(\mathbf{x}, E) \nabla \psi\} - \frac{\partial}{\partial E} \{b(E) \psi\} = q(\mathbf{x}, E) , \quad (1)$$

where  $\psi(\mathbf{x}, E)$  denotes the positron number density per unit energy and  $q(\mathbf{x}, E)$  is the positron source term. The transport through the magnetic turbulences is described by the space independent diffusion coefficient  $K(\mathbf{x}, E) = K_0 \epsilon^\delta$  where  $\epsilon = E/E_0$  and  $E_0 = 1$  GeV. Positrons lose energy through synchrotron radiation and inverse Compton scattering on the cosmic microwave background radiation and on the galactic starlight at a rate  $b(E) = E_0 \epsilon^2 / \tau_E$  where  $\tau_E = 10^{16}$  s. The diffusive halo inside which cosmic rays propagate before escaping

into the intergalactic medium is pictured as a flat cylinder with radius  $R_{\text{gal}} = 20$  kpc and extends along the vertical direction from  $z = -L$  up to  $z = +L$ . The gaseous disk lies in the middle at  $z = 0$  and contains the interstellar material on which most of the cosmic ray spallations take place. The half-thickness  $L$  is not constrained by the measurements of the boron to carbon ratio cosmic ray fluxes B/C. Its value could be anywhere in the interval between 1 and 15 kpc. As cosmic rays escape from that diffusive zone (DZ) and become scarce in the intergalactic medium, the density  $\psi$  is generally assumed to vanish at the radial boundaries  $r = R_{\text{gal}}$  and  $z = \pm L$ . Assuming steady state, the master equation (1) simplifies into

$$K_0 \epsilon^\delta \Delta \psi + \frac{\partial}{\partial \epsilon} \left\{ \frac{\epsilon^2}{\tau_E} \psi \right\} + q = 0 , \quad (2)$$

and may be solved by translating [8] the energy  $\epsilon$  into the pseudo-time

$$\tilde{t}(\epsilon) = \tau_E \left\{ v(\epsilon) = \frac{\epsilon^{\delta-1}}{1-\delta} \right\} . \quad (3)$$

In this formalism, the energy losses experienced by positrons are described as an evolution in the pseudo-time  $\tilde{t}$ . As a consequence, the propagation relation (2) simplifies into the heat equation

$$\frac{\partial \tilde{\psi}}{\partial \tilde{t}} - K_0 \Delta \tilde{\psi} = \tilde{q}(\mathbf{x}, \tilde{t}) , \quad (4)$$

where the space and energy positron density is now  $\tilde{\psi} = \epsilon^2 \psi$  whereas the positron production rate has become  $\tilde{q} = \epsilon^{2-\delta} q$ .

---

In the Green function formalism,  $G_{e^+}(\mathbf{x}, E \leftarrow \mathbf{x}_S, E_S)$  stands for the probability for a positron injected at  $\mathbf{x}_S$  with the energy  $E_S$  to reach the location  $\mathbf{x}$  with the degraded energy  $E \leq E_S$ , and the positron density is given by the convolution

$$\psi(\mathbf{x}, E) = \int_{E_S=E}^{E_S=+\infty} dE_S \int_{\text{DZ}} d^3 \mathbf{x}_S G_{e^+}(\mathbf{x}, E \leftarrow \mathbf{x}_S, E_S) q(\mathbf{x}_S, E_S) . \quad (5)$$

In the pseudo-time approach, the positron propagator may be expressed as

$$G_{e^+}(\mathbf{x}, E \leftarrow \mathbf{x}_S, E_S) = \frac{\tau_E}{E_0 \epsilon^2} \tilde{G}(\mathbf{x}, \tilde{t} \leftarrow \mathbf{x}_S, \tilde{t}_S) , \quad (6)$$

where  $\tilde{G}$  is the Green function associated to the heat equation (4). Without any boundary condition, this heat propagator would be given by the 3D expression

$$\tilde{G}(\mathbf{x}, \tilde{t} \leftarrow \mathbf{x}_S, \tilde{t}_S) = \left\{ \frac{1}{4\pi K_0 \tilde{\tau}} \right\}^{3/2} \exp \left\{ -\frac{(\Delta \mathbf{x})^2}{4 K_0 \tilde{\tau}} \right\} , \quad (7)$$

---

where  $\tilde{\tau} = \tilde{t} - \tilde{t}_S$  is the typical time including the diffusion process during which the positron energy decreases from  $E_S$  to  $E$ . The distance between the source  $\mathbf{x}_S$  and the observer  $\mathbf{x}$  is  $\Delta \mathbf{x}$  whereas the typical diffusion length associated to  $\tilde{\tau}$  is  $\lambda_D = \sqrt{4 K_0 \tilde{\tau}}$ . In order to implement the vertical boundary conditions  $\psi(\pm L) = 0$ , two approaches have been so far available.

(i) In the regime where the diffusion length  $\lambda_D$  is small with respect to the DZ half-thickness  $L$ , the method of the so-called electrical images consists in implementing

[8] an infinite series over the multiple reflections of the source as given by the vertical boundaries at  $+L$  and  $-L$ .

(ii) In the opposite regime, a large number of images needs to be considered and the convergence of the series is a problem. Fortunately, the diffusion equation along the vertical axis boils down to the Schrödinger equation – written in imaginary time – that accounts for the behaviour of a particle inside an infinitely deep 1D potential well that extends from  $z = -L$  to  $z = +L$ . The solution may be expanded as a series over the eigenstates of the corresponding Hamiltonian [10].

None of those methods deal with the radial boundaries at  $r = R_{\text{gal}}$ . The diffusive halo is here a mere infinite slab and not a flat cylinder. The Bessel approach which we present next remedies that problem and is an improvement with respect to the former Green formalism.

### A. The Bessel solution

As the DZ is axisymmetric and since we will consider spherically symmetric source terms only, we may expand

the cosmic ray density  $\psi(r, z, \epsilon)$  as the Bessel series

$$\psi(r, z, \epsilon) = \sum_{i=1}^{\infty} P_i(z, \epsilon) J_0(\alpha_i r / R_{\text{gal}}) . \quad (8)$$

Because the  $\alpha_i$ 's are the zeros of the Bessel function  $J_0$ , the cosmic ray density  $\psi$  systematically vanishes at the radial boundaries  $r = R_{\text{gal}}$ . The Bessel transforms  $P_i(z, \epsilon)$  fulfill the diffusion equation

$$K \partial_z^2 P_i - K \frac{\alpha_i^2}{R_{\text{gal}}^2} P_i + \frac{1}{\tau_E} \partial_\epsilon \{ \epsilon^2 P_i \} + Q_i(z, \epsilon) = 0. \quad (9)$$

---

The Bessel transform  $Q_i$  of the source distribution  $q$  is given by the usual expression

$$Q_i(z, \epsilon) = \frac{2}{R_{\text{gal}}^2} \frac{1}{J_1^2(\alpha_i)} \int_0^{R_{\text{gal}}} J_0(\alpha_i r / R_{\text{gal}}) q(r, z, \epsilon) r dr. \quad (10)$$


---

Each Bessel transform  $P_i(z, \epsilon)$  has to vanish at the boundaries  $z = -L$  and  $z = +L$  and may take any value in between. It can be therefore expanded as a Fourier series involving the basis of functions

$$\varphi_n(z) = \sin(n k_0 z') , \quad (11)$$

where  $k_0 = \pi/2L$  and  $z' = z + L$ . In our case, the DM distribution is symmetric with respect to the galactic plane and we can restrict ourselves to the functions  $\varphi_n(z)$  with odd  $n = 2m + 1$

$$\varphi_n(z) = (-1)^m \cos(n k_0 z) . \quad (12)$$


---

The Bessel transform  $P_i(z, \epsilon)$  is Fourier expanded as

$$P_i(z, \epsilon) = \sum_{n=1}^{\infty} P_{i,n}(\epsilon) \varphi_n(z) , \quad (13)$$

and the same expression holds for  $Q_i(z, \epsilon)$  for which we need to calculate explicitly the Fourier coefficient

$$Q_{i,n}(\epsilon) = \frac{1}{L} \int_{-L}^{+L} \varphi_n(z) Q_i(z, \epsilon) dz . \quad (14)$$

The Fourier transform of equation (9) involves the energy functions  $P_{i,n}(\epsilon)$  and  $Q_{i,n}(\epsilon)$

$$- K n^2 k_0^2 P_{i,n} - K \frac{\alpha_i^2}{R_{\text{gal}}^2} P_{i,n} + \frac{1}{\tau_E} \partial_\epsilon (\epsilon^2 P_{i,n}) + Q_{i,n}(z, \epsilon) = 0 . \quad (15)$$

At this stage, as for the Green approach, we can substitute the pseudo-time  $\tilde{t}$  for the energy  $\epsilon$ . By defining the new functions  $\tilde{P}_{i,n} = \epsilon^2 P_{i,n}$  and  $\tilde{Q}_{i,n} = \epsilon^{2-\delta} Q_{i,n}$ , we are led to the heat equation

$$\frac{d\tilde{P}_{i,n}}{d\tilde{t}} + \left\{ K_0 \left( n^2 k_0^2 + \frac{\alpha_i^2}{R_{\text{gal}}^2} \right) \right\} \tilde{P}_{i,n} = \tilde{Q}_{i,n} . \quad (16)$$

The solution to this ODE is straightforward

$$\tilde{P}_{i,n}(\tilde{t}) = \int_0^{\tilde{t}} \tilde{Q}_{i,n}(\tilde{t}_S) \exp\left\{-\tilde{C}_{i,n}(\tilde{t}-\tilde{t}_S)\right\} d\tilde{t}_S . \quad (17)$$

The argument of the exponential involves the diffusion length  $\lambda_D$  through the pseudo-time difference  $\tilde{\tau} = \tilde{t} - \tilde{t}_S$  as

$$\tilde{C}_{i,n}(\tilde{t}-\tilde{t}_S) = \left\{ \left(\frac{n\pi}{2L}\right)^2 + \frac{\alpha_i^2}{R_{\text{gal}}^2} \right\} K_0 \tilde{\tau} . \quad (18)$$

The cosmic ray positron density is given by the double expansion

$$\psi(r, z, \epsilon) = \sum_{i=1}^{\infty} \sum_{n=1}^{\infty} J_0(\alpha_i r/R_{\text{gal}}) \varphi_n(z) P_{i,n}(\epsilon) , \quad (19)$$

where

$$P_{i,n}(\epsilon) = \frac{\tau_E}{\epsilon^2} \int_{\epsilon}^{+\infty} Q_{i,n}(\epsilon_S) \exp\left\{-\tilde{C}_{i,n}(\tilde{t}-\tilde{t}_S)\right\} d\epsilon_S . \quad (20)$$

We eventually get the positron flux  $\Phi_{e^+} = \beta_{e^+} \psi(r, z, \epsilon)/4\pi$  where the positron velocity  $\beta_{e^+}$  depends on the energy  $\epsilon$ .

## B. The source term for primary positrons

Let us now consider the source term  $q(\mathbf{x}, E)$  of the master equation (1). We are here interested in primary positrons, namely the ones that are produced by the pair annihilations of DM particles. According to the various supersymmetric theories, the annihilation of a DM pair leads either to the direct creation of an electron-positron pair or to the production of many species subsequently decaying into photons, neutrinos, hadrons and positrons. We have considered four possible annihilation channels which appear in any model of weakly interacting massive particles (WIMP). The first one is the direct production of a  $e^+e^-$  pair and is actually generic for theories with extra-dimensions like the UED models [13, 14, 15]. The energy of the positron line corresponds to the mass of the DM species. We have alternatively considered annihilations into  $W^+W^-$ ,  $\tau^+\tau^-$  and  $b\bar{b}$  pairs. These unstable particles decay and produce showers which may contain positrons with a continuous energy spectrum. Whichever the annihilation channel, the source term can be generically written as

$$q(\mathbf{x}, E) = \eta \langle \sigma v \rangle \left\{ \frac{\rho(\mathbf{x})}{m_\chi} \right\}^2 f(\epsilon) . \quad (21)$$

The coefficient  $\eta$  is a quantum term which depends on the particle being or not self-conjugate : for instance, for a fermion it equals 1/2 or 1/4 depending on whether the WIMP is a Majorana or a Dirac particle. In what follows, we have considered a Majorana type species and taken  $\eta = 1/2$ . The annihilation cross section is averaged over the momenta of the incoming DM particles to yield  $\langle \sigma v \rangle$ , the value of which depends on the specific SUSY model and is constrained by cosmology. We have actually taken here a benchmark value of  $2.1 \times 10^{-26} \text{ cm}^3 \text{ s}^{-1}$  which leads to a relic abundance of  $\Omega_\chi h^2 \sim 0.14$  (in agreement with the WMAP observations) under the hypothesis of dominant s-wave annihilation and by means of the relation:

$$\Omega h^2 = 8.5 \cdot 10^{-11} \frac{g_*^{1/2}(x_f)}{g_{*S}(x_f)} \frac{\text{GeV}^{-2}}{x_{f-1} \langle \sigma v \rangle} = \frac{3 \cdot 10^{-27} \text{ cm}^3 \text{ s}^{-1}}{\langle \sigma v \rangle} \quad (22)$$

where  $x_f = m_\chi/T_f \simeq (20 \div 25)$  with  $T_f$  the freeze-out temperature and where  $g_*(x_f)$  and  $g_{*S}(x_f)$  denote the effective number of degrees of freedom of the energy and entropy density at freeze-out, respectively.

The DM mass  $m_\chi$  is unknown. In the case of neutralinos, theoretical arguments as well as the LEP and WMAP results constrain this mass to range from a few GeV [16, 17, 18, 19] up to a few TeV. Keeping in mind the positron HEAT excess, we have chosen a neutralino mass of 100 GeV. We have also analyzed the positron signal yielded by a significantly heavier DM particle of 500 GeV. Finally, the energy distribution of the positrons produced in a single WIMP annihilation is denoted by  $f(\epsilon) \equiv dN_{e^+}/dE_{e^+}$  and has been evaluated with the help of the Pythia Monte-Carlo [20].

The only astronomical ingredient in the source term (21) is the DM distribution  $\rho(\mathbf{x})$  inside the Milky Way halo. We have considered the generic profile

$$\rho(r) = \rho_\odot \left\{ \frac{r_\odot}{r} \right\}^\gamma \left\{ \frac{1 + (r_\odot/r_s)^\alpha}{1 + (r/r_s)^\alpha} \right\}^{(\beta-\gamma)/\alpha} , \quad (23)$$

where  $r_\odot = 8.5 \text{ kpc}$  is the galactocentric distance of the solar system. Notice that  $r$  denotes here the radius in spherical coordinates. The solar neighborhood DM density has been set equal to  $\rho_\odot = 0.3 \text{ GeV cm}^{-3}$ . Three profiles have been discussed in this work : an isothermal cored distribution [21] for which  $r_s$  is the radius of the central core, the Navarro, Frenk and White profile [22]

Halo model	$\alpha$	$\beta$	$\gamma$	$r_s$ [kpc]
Cored isothermal [21]	2	2	0	5
Navarro, Frenk & White [22]	1	3	1	20
Moore [23]	1.5	3	1.3	30

TABLE I: Dark matter distribution profiles in the Milky Way.

(hereafter NFW) and Moore’s model [23]. The NFW and Moore profiles have been numerically established thanks to N-body simulations. In the case of the Moore profile, the index  $\gamma$  lies between 1 and 1.5 and we have chosen a value of 1.3 – see Tab. I. The possible presence of DM substructures inside those smooth distributions enhances the annihilation signals by the so-called boost factor whose value is still open to debate.

The positron flux at the Earth may be expressed as

$$\Phi_{e^+} = \frac{\beta_{e^+}}{4\pi} \{ \psi(\odot, \epsilon) \equiv \kappa \frac{\tau_E}{c^2} \int_{\epsilon}^{+\infty} d\epsilon_S f(\epsilon_S) \tilde{I}(\lambda_D) \}, \quad (24)$$

Alternatively, in the Bessel approach, the halo integral  $\tilde{I}$  is given by the radial and vertical expansions

$$\tilde{I}(\lambda_D) = \sum_{i=1}^{\infty} \sum_{n=1}^{\infty} J_0(\alpha_i r / R_{\text{gal}}) \varphi_n(z) \exp \left\{ -\tilde{C}_{i,n} (\tilde{t} - \tilde{t}_S) \right\} R_{i,n} , \quad (28)$$

where the coefficients  $R_{i,n}$  are the Bessel and Fourier transforms of the DM density squared  $(\rho/\rho_{\odot})^2$ .

We insist again on the fact that the true argument of the halo function, whatever the approach followed to derive it, is the positron diffusion length  $\lambda_D$ . This integral encodes the information relevant to cosmic ray propagation through the height  $L$  of the diffusive zone, the normalization  $K_0$  of the diffusion coefficient and its spectral index  $\delta$ . It is also the only relevant quantity concerning the DM distribution. The analysis of the various astrophysical uncertainties that may affect the positron signal of annihilating WIMPs will therefore be achieved by studying the behavior of  $\tilde{I}$ .

### C. The Bessel method versus the Green approach

The diffusive halo integral  $\tilde{I}(\lambda_D)$  may be calculated by using either the Bessel expansion method or the Green function approach. We investigate here the relevance of each as a function of the diffusion length  $\lambda_D$ .

To commence, the DM distribution is taken in Fig. 1 to be constant throughout the diffusive zone with  $\rho = \rho_{\odot}$ . Both methods – Green or Bessel – do not give the same result as soon as  $L$  is large enough. Neglecting the radial

where the information pertinent to particle physics has been factored out in

$$\kappa = \eta \langle \sigma v \rangle \left\{ \frac{\rho_{\odot}}{m_{\chi}} \right\}^2 . \quad (25)$$

The diffusive halo integral  $\tilde{I}$  depends on the input energy  $\epsilon_S$  and on the observed energy  $\epsilon$  through the diffusion length  $\lambda_D$  given by

$$\lambda_D^2 = 4K_0\tau_E \left\{ \frac{\epsilon^{\delta-1} - \epsilon_S^{\delta-1}}{1 - \delta} \right\} . \quad (26)$$

In the Green formalism, the halo function  $\tilde{I}$  may be expressed as the convolution of the reduced propagator  $\tilde{G}$  – see Eq. (6) and (7) – with the DM density squared  $(\rho/\rho_{\odot})^2$  over the diffusive zone

$$\tilde{I}(\lambda_D) = \int_{\text{DZ}} d^3\mathbf{x}_S \tilde{G}(\odot, \epsilon \leftarrow \mathbf{x}_S, \epsilon_S) \left\{ \frac{\rho(\mathbf{x}_S)}{\rho_{\odot}} \right\}^2 . \quad (27)$$

boundary condition – the cosmic ray density vanishes at  $r = R_{\text{gal}}$  – leads to overestimate the halo function  $\tilde{I}$  when the diffusion slab is thick. This can be easily understood : if the slab is thin enough, a positron created near the radial boundary has a large probability to hit the vertical borders of the diffusive zone at  $\pm L$  and hereby to escape into the intergalactic medium, never reaching the Earth. If so, the positron horizon does not reach radially the outskirts of the diffusive zone and the Green approach (long dashed curves) provides a very good approximation to the correct value of  $\tilde{I}$  as given by the Bessel expansion (solid lines). Conversely, if the slab is thick, we detect at the Earth a non negligible fraction of positrons produced near the radial boundary and the Green approximation is no longer acceptable. This is particularly true for the red curves of the  $L = 20$  kpc case where the Green result largely overestimates the exact value. This justifies the use of the Bessel expansion method which improves upon the previous treatments of positron propagation and is one of the novelties of this article.

As already discussed, a change in the normalization  $K_0$  or in the index  $\delta$  of the cosmic ray diffusion coefficient leads only to a variation of the diffusion length  $\lambda_D$

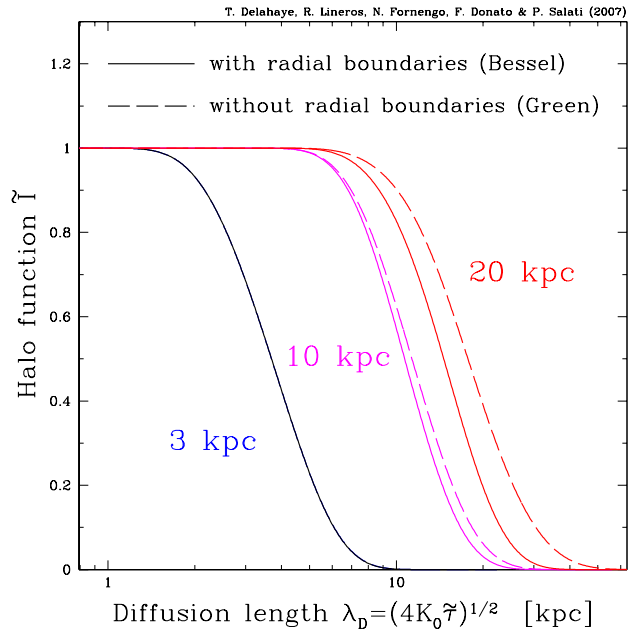


FIG. 1: Influence of the radial boundary condition for a slab half-thickness  $L$  of 3, 10 and 20 kpc ( $R_{\text{gal}} = 20$  kpc). The thicker the slab, the larger the error when neglecting the radial boundary. On the contrary, for small values of  $L$ , positrons produced near the radial outskirts of the diffusive halo escape into the intergalactic medium and do not contribute to the signal at the Earth. Implementing correctly the radial boundary condition is not relevant in that regime.

through which those parameters appear. Notice that the relation that links the diffusion length  $\lambda_D$  to the diffusive zone integral  $\tilde{I}$  is not affected by those modifications. On the contrary, the half-thickness  $L$  of the diffusive slab has a direct influence on the overall shape of  $\tilde{I}$  as a function of  $\lambda_D$  as is clear in Fig. 2. In the left panel an isothermal distribution has been assumed whereas the right panel features the case of a NFW profile. For small values of  $L$  – see the green curve for which  $L = 1$  kpc – the positron horizon is fairly limited. Because the positrons detected at the Earth merely originate from a very near region, the DM profile which we probe is essentially uniform. As in Fig. 1, the DZ integral  $\tilde{I}$  is unity below  $\lambda_D \sim L$  and collapses for larger values of the diffusion length. For a thicker slab, the cosmic ray positron flux at the Earth gets sensitive to the center of the galaxy. That is why the halo integral  $\tilde{I}$  exhibits a maximum for a diffusion length  $\sim 5 - 7$  kpc, a value close to the galactocentric distance  $r_{\odot} = 8.5$  kpc of the solar system. In both panels, the larger  $L$ , the more visible the bump. Notice also that the steeper the DM profile, the higher the maximum. The curves featured in Fig. 2 point towards the importance of calculating correctly the influence of the

DM located at the galactic center, when  $L$  is large. We therefore need to assess the relative merits of the Bessel and Green approaches in doing so.

To achieve that goal, we have selected Moore’s model with a very steep and dense DM central distribution. In the left panel of Fig. 3, the dashed curves are obtained by the Green method. The convolution (27) is numerically calculated by summing over the grid of elementary cells into which the diffusive halo has been split. The resolution of that grid matters. For very small cells, the correct behavior of  $\tilde{I}$  is recovered and the dashed black curve is superimposed on the solid red line of the exact result derived with the Bessel expansion technique. However, the price to pay is an unacceptable CPU time. We had actually to break the inner 1 kpc into  $8 \times 10^5$  cells in order for the integral (27) to converge. When the resolution of the grid is relaxed by increasing the size of the Green cells, the bump is dramatically underestimated. This is especially clear for the dashed blue curve (labeled poor) where the DZ grid contains only a few  $10^4$  cells. On the other hand, notice that even in that case, the correct result is obtained for a diffusion length smaller than  $\sim 3$  kpc. In the right panel, we have concentrated on the Bessel method and numerically calculated the expansion (28). We have performed the summation up to a Bessel order of  $N_{\text{Bessel}}$  and a Fourier order of  $N_{\text{harmonic}}$ . The exact result – featured by the solid red curve – incorporates a large number of modes and is once again obtained at the price of a long CPU time. If the expansion (28) is truncated earlier – see the dashed blue line – we observe that the correct value of  $\tilde{I}$  is completely missed when the diffusion length is small. In that regime, the positrons that are detected at the Earth originate mostly from the solar neighborhood. A large number  $N_{\text{Bessel}}$  of radial modes is needed in order for the Bessel transforms  $R_{i,n}$  to interfere destructively with each other so that the influence of the galactic center is erased. For larger values of  $\lambda_D$ , the exponential terms in Eq. (28) force the series over  $R_{i,n}$  to converge rapidly. The exact value of the halo integral  $\tilde{I}$  can be recovered even with as few terms as 10 Bessel modes and 20 Fourier harmonics. Notice how well the peak at  $\lambda_D \sim 7$  kpc is reproduced by all the curves, whatever  $N_{\text{Bessel}}$  and  $N_{\text{harmonic}}$ . This peak was obtained with difficulty in the Green function approach. We therefore strongly advise to use the Green method as long as  $\lambda_D$  is smaller than  $\sim 3$  kpc whereas the Bessel expansion technique should be preferred above that value. This prescription allows a fast and accurate evaluation of the halo function  $\tilde{I}$ . We can safely embark on an extensive scan of the cosmic ray propagation parameters and assess the theoretical uncertainties that may affect the positron DM signal at the Earth.

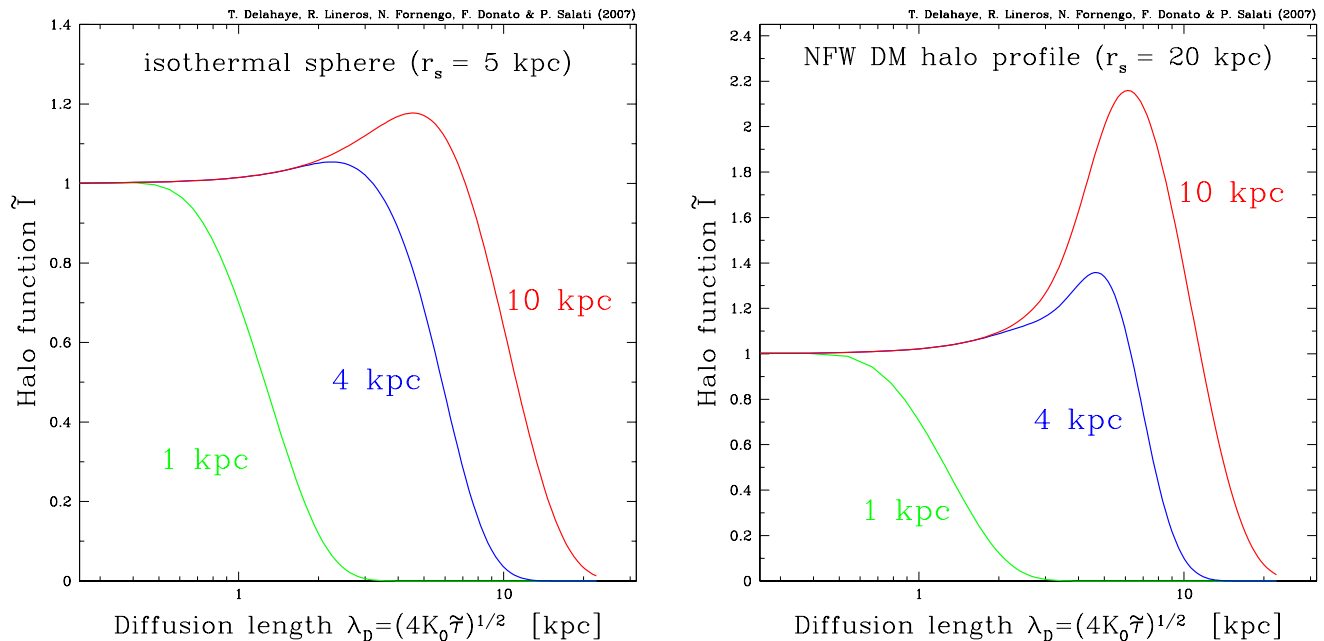


FIG. 2: The halo convolution  $\tilde{I}$  is plotted as a function of the diffusion length  $\lambda_D$  for various values of the slab half-thickness  $L$ . The left panel features the case of an isothermal DM distribution whereas a NFW profile has been assumed in the right panel – see Tab. I. When  $L$  is large enough for the positron horizon to reach the galactic center and its denser DM distribution, a maximum appears in the curves for  $\lambda_D \sim r_\odot$ .

#### D. The central divergence

Numerically derived DM profiles – NFW and Moore – exhibit a divergence at the center of the Milky Way. The density increases like  $r^{-\gamma}$  for small radii – see Eq. (23) – but cannot exceed the critical value for which the WIMP annihilation timescale is comparable to the age of the galactic bulge. The saturation of the density typically occurs within a sphere of  $\sim 10^{-7}$  pc, a much shorter distance than the space increment in the numerical integrals, *i.e.*, the Green convolution (5) and relations (10) and (14) for the Bessel expansion technique. Fortunately, this numerical difficulty can be eluded by noticing that the Green propagator  $G_{e^+}(\odot, \epsilon \leftarrow r \sim 0, \epsilon_S)$  which connects the inner Galaxy to the Earth does not vary much over the central DM distribution. This led us to replace inside a sphere of radius  $r_0$  the  $r^{-\gamma}$  cusp with the smoother profile

$$\rho^*(r) = \rho_0 \{1 + a_1 \text{sinc}(\pi x) + a_2 \text{sinc}(2\pi x)\}^{1/2}, \quad (29)$$

where  $x = r/r_0$  is the reduced radius. The coefficients  $\rho_0$ ,  $a_1$  and  $a_2$  are obtained by requiring that both the smooth density  $\rho^*$  and its first derivative  $d\rho^*/dr$  are continuous at  $r_0$ . The other crucial condition is the conservation of the total number of annihilations within  $r_0$  as the diverging cusp  $\rho \propto r^{-\gamma}$  is replaced by the distribution  $\rho^*$ .

These conditions imply that  $\rho_0 \equiv \rho(r_0)$  whereas

$$a_1 = a_2 + 2\gamma, \quad (30)$$

$$a_2 = 8\gamma \left\{ \frac{\pi^2 - 9 + 6\gamma}{9(3 - 2\gamma)} \right\}. \quad (31)$$

In Fig. 4, the halo integral  $\tilde{I}$  is plotted as a function of the diffusion length  $\lambda_D$  in the case of the Moore profile and assuming a slab half-thickness  $L = 10$  kpc. Within the radius  $r_0$ , the central DM divergence has been replaced either by a plateau with constant density  $\rho_0$  or by the renormalized profile (29). In the case of the plateau, the maximum which  $\tilde{I}$  reaches for a diffusion length  $\lambda_D \sim 7$  kpc is underestimated even if values as small as 100 pc are assumed for  $r_0$ . The larger that radius, the fewer the annihilations taking place within  $r_0$  as compared to the Moore cusp and the worse the miscalculation of the halo integral. Getting the correct result featured by the solid red line would require a plateau radius so small that the CPU time would explode. On the contrary, we observe that the halo integral  $\tilde{I}$  is stable with respect to a change of  $r_0$  when the renormalized density  $\rho^*$  is used.

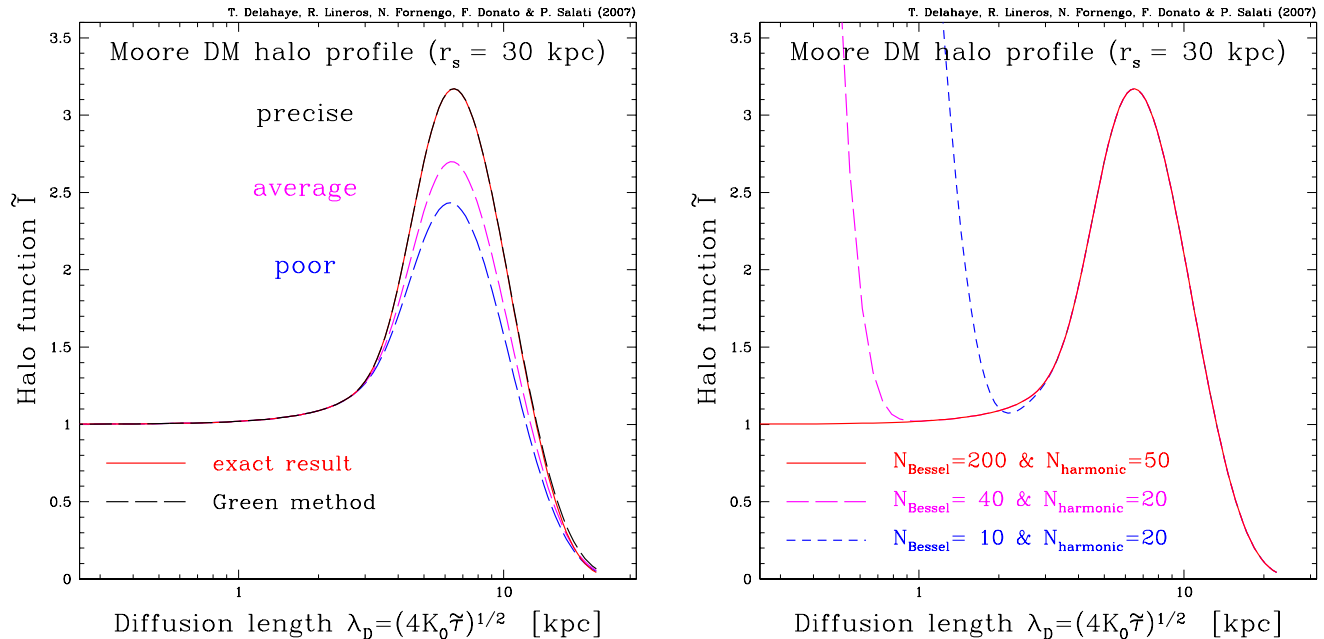


FIG. 3: The halo integral  $\tilde{I}$  is plotted as a function of the diffusion length  $\lambda_D$  in the case of a Moore profile with  $L = 10$  kpc. In the left panel, the results obtained with the Green function method are featured by the long-dashed curves and may be compared to the exact solution and its solid red line. In the right panel, the numbers  $N_{\text{Bessel}}$  and  $N_{\text{harmonic}}$  of the eigenfunctions considered in the Bessel expansion (28) have been varied. The various curves reproduce astonishingly well the bump but diverge at small  $\lambda_D$  when too few Bessel and Fourier terms are considered.

### III. PROPAGATION UNCERTAINTIES ON THE HALO INTEGRAL

Following the prescription which has been given in the previous section, we can calculate accurately and quickly the halo integral  $\tilde{I}$  using either the Green propagator method or the Bessel expansion technique according to the typical diffusion length  $\lambda_D$ . We are now equipped with a rapid enough method for scanning the  $\sim 1,600$  different cosmic ray propagation models that have been found compatible [12] with the B/C measurements. Each model is characterized by the half-thickness  $L$  of the diffusion zone and by the normalization  $K_0$  and spectral index  $\delta$  of the space diffusion coefficient. A large variation in these parameters is found in [12] and yet they all lead to the same B/C ratio. The height  $L$  of the diffusion slab lies in the range from 1 to 15 kpc. Values of the spectral index  $\delta$  extend from 0.46 to 0.85 whereas the ratio  $K_0/L$  varies from  $10^{-3}$  to  $8 \times 10^{-3}$  kpc Myr $^{-1}$ .

In this section, we analyze the sensitivity of the positron halo integral  $\tilde{I}$  with respect to galactic propagation. We would like eventually to gauge the astrophysical uncertainties which may affect the predictions on the positron DM signal. A similar investigation – with only the propagation configurations that survive the B/C test – has already been carried out for secondary [25] and

Model	$\delta$	$K_0$ [kpc $^2$ /Myr]	$L$ [kpc]
MIN	0.85	0.0016	1
MED	0.70	0.0112	4
MAX	0.46	0.0765	15

TABLE II: Typical combinations of cosmic ray propagation parameters that are compatible with the B/C analysis [12] and which have been found [24] to correspond respectively to minimal, medium and maximal primary antiproton fluxes.

primary [24] antiprotons. In the later case, three specific sets of parameters have been derived corresponding to minimal, medium and maximal antiproton fluxes – see Tab. II.

Do these configurations play the same role for positrons? Can we single out a few propagation models which could be used later on to derive the minimal or the maximal positron flux without performing an entire scan over the parameter space? These questions have not been addressed in the pioneering investigation of [9] where the cosmic ray propagation parameters have indeed been varied but independently of each other and without any connection to the B/C ratio.

In Fig. 5, we have set the positron detection energy  $E$  at a fixed value of 10 GeV and varied the injection energy

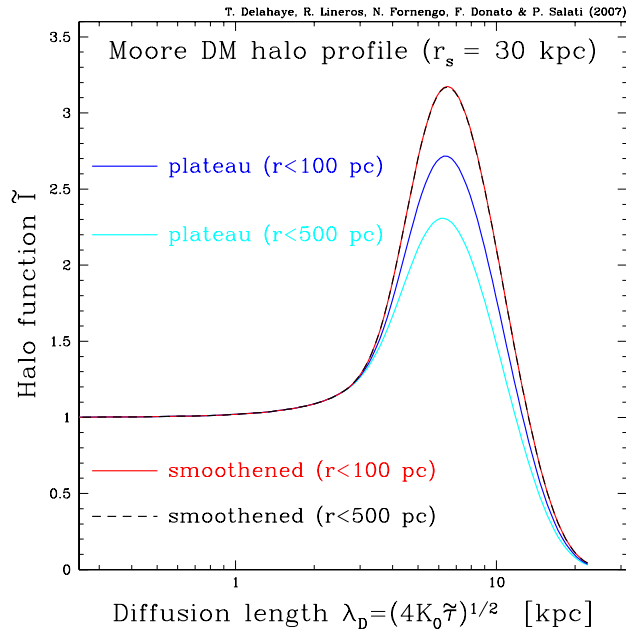


FIG. 4: Same plot as before where the central DM profile within a radius  $r_0$  is either a plateau at constant density  $\rho_0$  or the smooth distribution  $\rho^*$  of Eq. (29). In the former case, the bump which  $\tilde{I}$  exhibits is significantly underestimated even for values of  $r_0$  as small as 100 pc – solid dark blue – and drops as larger values are considered – solid light blue. On the contrary, if the DM cusp is replaced by the smooth profile  $\rho^*$ , the halo integral no longer depends on the renormalization radius  $r_0$  and the solid red and long-dashed black curves are superimposed on each other.

$E_S$  from 10 GeV up to 1 TeV. The three panels correspond to the DM halo profiles of Tab. I. For each value of the injection energy  $E_S$ , we have performed a complete scan over the 1,600 different configurations mentioned above and have found the maximal and minimal values of the halo integral  $\tilde{I}$  with the corresponding sets of propagation parameters. In each panel, the resulting uncertainty band corresponds to the yellow region extending between the two solid red lines. The lighter yellow domain is demarcated by the long-dashed black curves labeled MIN and MAX and has a smaller spread. The MED configuration is featured by the long-dashed blue line. In Fig. 6, the Moore profile has been chosen with four different values of the detection energy  $E$ . The corresponding uncertainty bands are coded with different colors and encompass each other as  $E$  increases.

As  $E_S$  gets close to  $E$ , we observe that each uncertainty domain shrinks. In that regime, the diffusion length  $\lambda_D$  is very small and the positron horizon probes only the solar neighborhood where the DM density is given by  $\rho_\odot$ . Hence the flagellate structure of Fig. 6 and a halo integral  $\tilde{I}$  of order unity whatever the propagation model.

As is clear in Fig. 2, a small half-thickness  $L$  of the diffusion slab combined with a large diffusion length  $\lambda_D$  implies a small positron halo integral  $\tilde{I}$ . The lower boundaries of the various uncertainty bands in Fig. 5 and 6 correspond therefore to parameter sets with  $L = 1$  kpc. Large values of  $\lambda_D$  are obtained when both the normalization  $K_0$  and the spectral index  $\delta$  are large – see Eq. (26). However both conditions cannot be satisfied together once the B/C constraints are applied. For a large normalization  $K_0$ , only small values of  $\delta$  are allowed and vice versa. For small values of the detection energy  $E$ , the spectral index  $\delta$  has little influence on  $\lambda_D$  and the configuration which minimizes the halo integral  $\tilde{I}$  corresponds to the large normalization  $K_0 = 5.95 \times 10^{-3} \text{ kpc}^2 \text{ Myr}^{-1}$  and the rather small  $\delta = 0.55$ . For large values of  $E$ , the spectral index  $\delta$  becomes more important than  $K_0$  in the control of  $\lambda_D$ . That is why in Fig. 6, the lower bound of the red uncertainty domain corresponds now to the small normalization  $K_0 = 1.65 \times 10^{-3} \text{ kpc}^2 \text{ Myr}^{-1}$  and the large spectral index  $\delta = 0.85$ . Notice that this set of parameters is very close to the MIN configuration of Tab. II. For intermediate values of  $E$ , the situation becomes more complex. We find in particular that for  $E = 30$  GeV, the halo integral  $\tilde{I}$  is minimal for the former set of parameters as long as  $E_S \leq 200$  GeV and for the later set as soon as  $E_S \geq 230$  GeV. In between, a third propagation model comes into play with the intermediate values  $K_0 = 2.55 \times 10^{-3} \text{ kpc}^2 \text{ Myr}^{-1}$  and  $\delta = 0.75$ . It is not possible therefore to single out one particular combination of  $K_0$  and  $\delta$  which would lead to the minimal value of the halo integral and of the positron DM signal. The MIN configuration which appeared in the antiproton analysis has no equivalent for positrons.

The same conclusion holds, even more strongly, in the case of the upper boundaries of the uncertainty bands. Whatever the DM halo profile, the panels of Fig. 2 feature a peak in the halo function  $\tilde{I}$  for large values of  $L$  and for a specific diffusion length  $\lambda_D^{\text{max}} \sim 7$  kpc. At fixed  $E$  and  $E_S$ , we anticipate that the maximal value for  $\tilde{I}$  will be reached for  $L = 15$  kpc and for a diffusion length  $\lambda_D$  as close as possible to the peak value  $\lambda_D^{\text{max}}$ . Two regimes can be considered at this stage.

(i) To commence, the diffusion length  $\lambda_D$  is below the critical value  $\lambda_D^{\text{max}}$  whenever the difference  $v(\epsilon) - v(\epsilon_S)$  is small enough – see the definitions (3) and (26). This condition is met in general when  $E$  and  $E_S$  are close to each other or when  $E$  is large. The largest possible value of  $\lambda_D$  maximizes  $\tilde{I}$  and once again, we find two propagation models. For small  $E$ , the large normalization  $K_0 = 7.65 \times 10^{-2} \text{ kpc}^2 \text{ Myr}^{-1}$  is preferred with  $\delta = 0.46$ . We recognize the MAX configuration of Tab. II and understand why the long-dashed black curves labeled MAX in the panels of Fig. 5 are superimposed on the solid

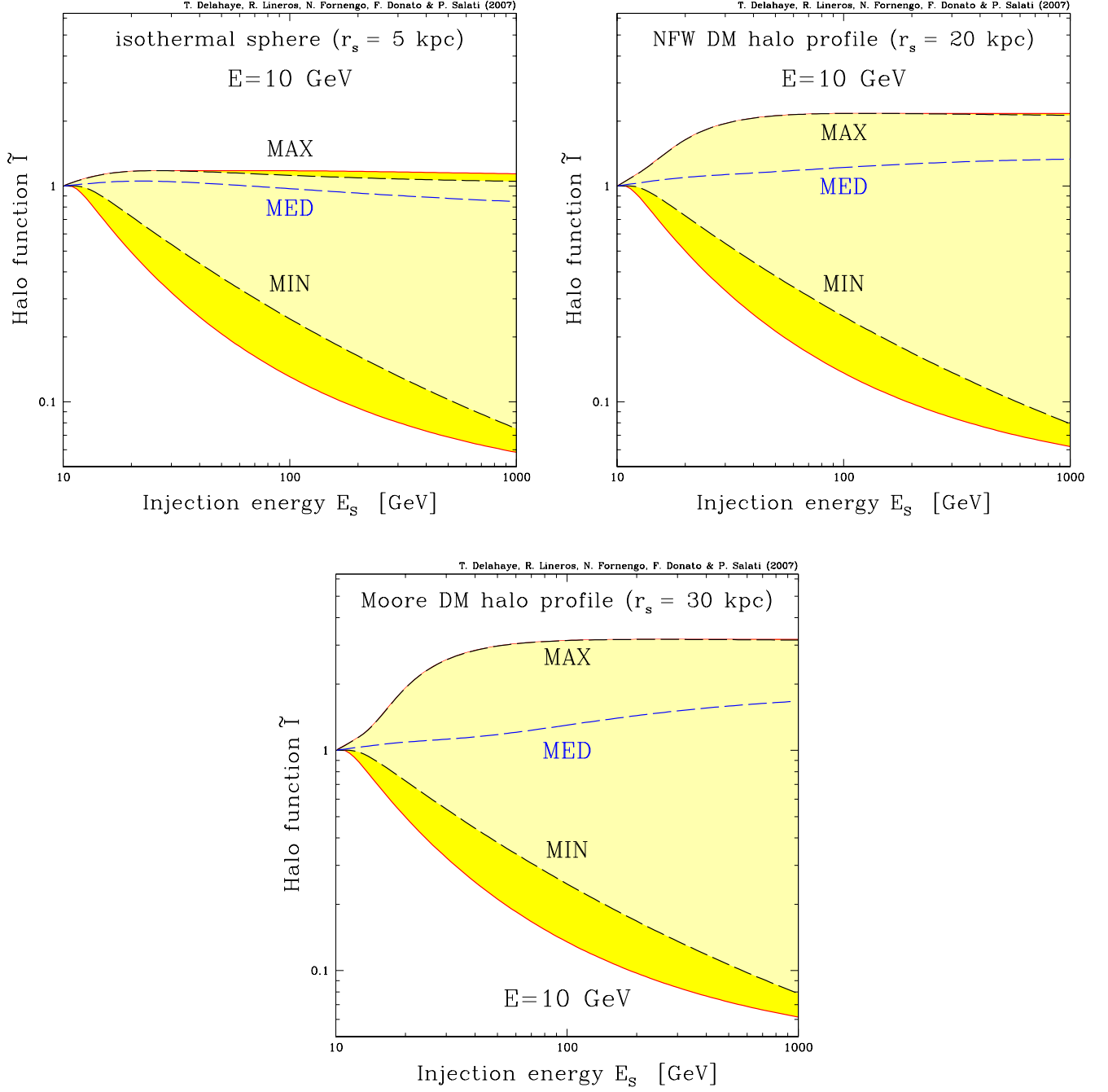


FIG. 5: In each panel, the halo integral  $\tilde{I}$  is plotted as a function of the positron injection energy  $E_S$  whereas the energy  $E$  at the Earth is fixed at 10 GeV. The galactic DM halo profiles of Tab. I are featured. The curves labeled as MED correspond to the choice of cosmic ray propagation parameters which best-fit the B/C ratio [12]. The MAX and MIN configurations correspond to the cases which were identified to produce the maximal and minimal DM antiproton fluxes [24], while the entire colored band corresponds to the complete set of propagation models compatible with the B/C analysis [12].

red upper boundaries. For large  $E$ , the spectral index  $\delta$  dominates the diffusion length  $\lambda_D$  and takes over the normalization  $K_0$  of the diffusion coefficient. The best model which maximizes  $\tilde{I}$  becomes then  $\delta = 0.75$  and  $K_0 = 2.175 \times 10^{-2} \text{ kpc}^2 \text{ Myr}^{-1}$ .

(ii) When the difference  $v(\epsilon) - v(\epsilon_S)$  is large enough, the diffusion length  $\lambda_D$  may reach the critical value  $\lambda_D^{\text{max}}$  for at least one propagation model which therefore maximizes the halo integral. As  $E$  and  $E_S$  are varied, the peak value of  $\tilde{I}$  is always reached when a scan through

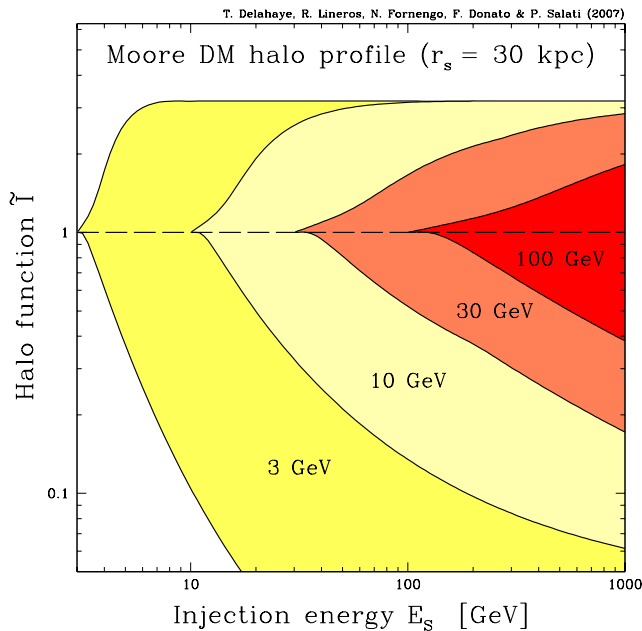


FIG. 6: Same plot as before where the Moore DM profile has been selected. Four values of the positron detection energy  $E$  have been assumed. The flagella structure of this figure results from the widening of the uncertainty band as the detection energy  $E$  is decreased.

the space of parameters is performed. This peak value corresponds to the maximum of the halo integral, hence a horizontal upper boundary for each of the uncertainty bands of Fig. 5 and 6. The set that leads to  $\lambda_D = \lambda_D^{\max}$  is different for each combination of  $E$  and  $E_S$  and is not unique. In the case of the NFW DM profile of Fig. 5, the halo integral  $\tilde{I}$  is maximized by more than 30 models above  $E_S = 120$  GeV.

The complexity of this analysis confirms that the propagation configurations selected by B/C do not play the same role for primary antiprotons and positrons. The two species experience the propagation phenomena, and in particular energy losses, with different intensities. As pointed out in Ref. [26], the average distance traveled by a positron is sensibly lower than the one experienced by an antiproton produced in the halo.

#### IV. POSITRON FLUXES

Now that we have discussed in detail the solution of the propagation equation, and have identified and quantified the astrophysical uncertainties on the halo integral  $\tilde{I}$ , we are ready to apply our analysis to the theoretical predictions for the positron signal at the Earth position. The positron flux is obtained through Eq. (24).

As stated in Sec. II B, we will not adopt specific DM candidates, but will instead discuss the signals arising from a DM particle which annihilates into a pure final state. We consider four different specific DM annihilation channels: direct  $e^+e^-$  production as well as  $W^+W^-$ ,  $b\bar{b}$  and  $\tau^+\tau^-$ . The DM annihilation cross section is fixed at the value  $2.1 \times 10^{-26} \text{ cm}^3 \text{ s}^{-1}$  and we will consider the cases of a DM species with mass of 100 GeV and of 500 GeV. Generic DM candidates, for instance a neutralino or a sneutrino in supersymmetric models, or the lightest Kaluza–Klein particle in models with extra–dimensions, will entail annihilation processes with specific branching ratios into one or more of these benchmark cases. The positron flux in these more general situations would simply be a superposition of the results for each specific annihilation channel, weighted by the relevant branching ratios and normalized by the actual annihilation cross section.

Model	$\delta$	$K_0$ [kpc <sup>2</sup> /Myr]	$L$ [kpc]
MED	0.70	0.0112	4
M1	0.46	0.0765	15
M2	0.55	0.00595	1

TABLE III: Typical combinations of cosmic ray propagation parameters that are compatible with the B/C analysis [12]. The model MED has been borrowed from Tab. II. Models M1 and M2 respectively maximize and minimize the positron flux over some energy range – roughly above 10 GeV – the precise extent of which depends on the mass of the DM particle, on the annihilation channel and also on the DM profile. Note that M1 is the same as MAX in Tab. II but this is coincidental.

In Fig. 7, the propagated positron flux  $\Phi_{e^+}$  – multiplied by the square of the positron energy  $E$  for convenience – is featured as a function of  $E$  for a 100 GeV DM particle and a NFW density profile. The colored [yellow] area corresponds to the total uncertainty band arising from positron propagation. In all panels, it enlarges at low positron energy. This may be understood as a consequence of the behavior of the halo integral  $\tilde{I}$  which was analyzed in Sec. III. Positrons produced at energy  $E_S$  and detected at energy  $E$  originate on average from a sphere whose radius is  $\lambda_D$ . That positron sphere enlarges as  $E$  decreases and so does the uncertainty band. As positrons originate further from the Earth, the details of galactic propagation become more important in the determination of the positron flux. On the contrary, high–energy positrons are produced locally and the halo integral  $\tilde{I}$  becomes unity whatever the astrophysical parameters. Notice also that the uncertainty band can be sizeable and depends significantly on the positron spectrum at production. In the case of the  $e^+e^-$  line of

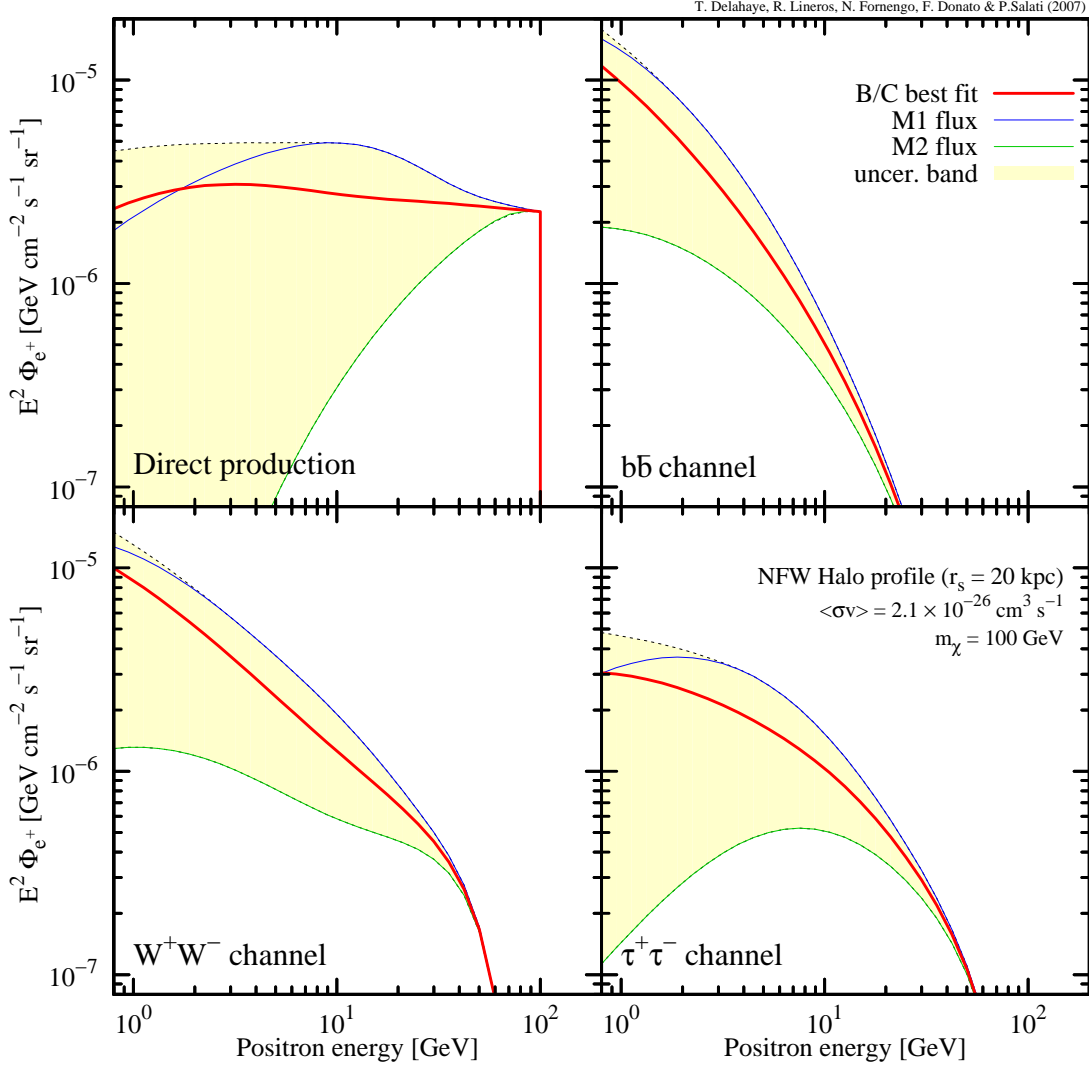


FIG. 7: Positron flux  $E^2\Phi_{e^+}$  versus the positron energy  $E$ , for a DM particle with a mass of 100 GeV and for a NFW profile – see Tab. I. The four panels refer to different annihilation final states : direct  $e^+e^-$  production (top left),  $b\bar{b}$  (top right),  $W^+W^-$  (bottom left) and  $\tau^+\tau^-$  (bottom right). In each panel, the thick solid [red] curve refers to the best-fit choice (MED) of the astrophysical parameters. The upper [blue] and lower [green] thin solid lines correspond respectively to the astrophysical configurations which provide here the maximal (M1) and minimal (M2) flux – though only for energies above a few GeV in the case of (M1). The colored [yellow] area features the total uncertainty band arising from positron propagation.

the upper left panel, the positron flux  $\Phi_{e^+}$  exhibits a strongly increasing uncertainty as  $E$  is decreased from  $m_\chi$  down to 1 GeV. That uncertainty is one order of magnitude at  $E = 10$  GeV, and becomes larger than 2 orders of magnitude below 1 GeV. Once again, the positron sphere argument may be invoked. At fixed detected energy  $E$ , the radius  $\lambda_D$  increases with the injected energy  $E_S$ . We therefore anticipate a wider uncertainty band as the source spectrum gets harder. This trend is clearly

present in the panels of Fig. 7. Actually direct production is affected by the largest uncertainty, followed by the  $\tau^+\tau^-$  and  $W^+W^-$  channels where a positron is produced either directly from the  $W^+$  or from the leptonic decays. In the  $b\bar{b}$  case, which is here representative of all quark channels, a softer spectrum is produced since positrons arise mostly from the decays of charged pions originating from the quark hadronization. Most of the positrons have already a low energy  $E_S$  at injection and since they

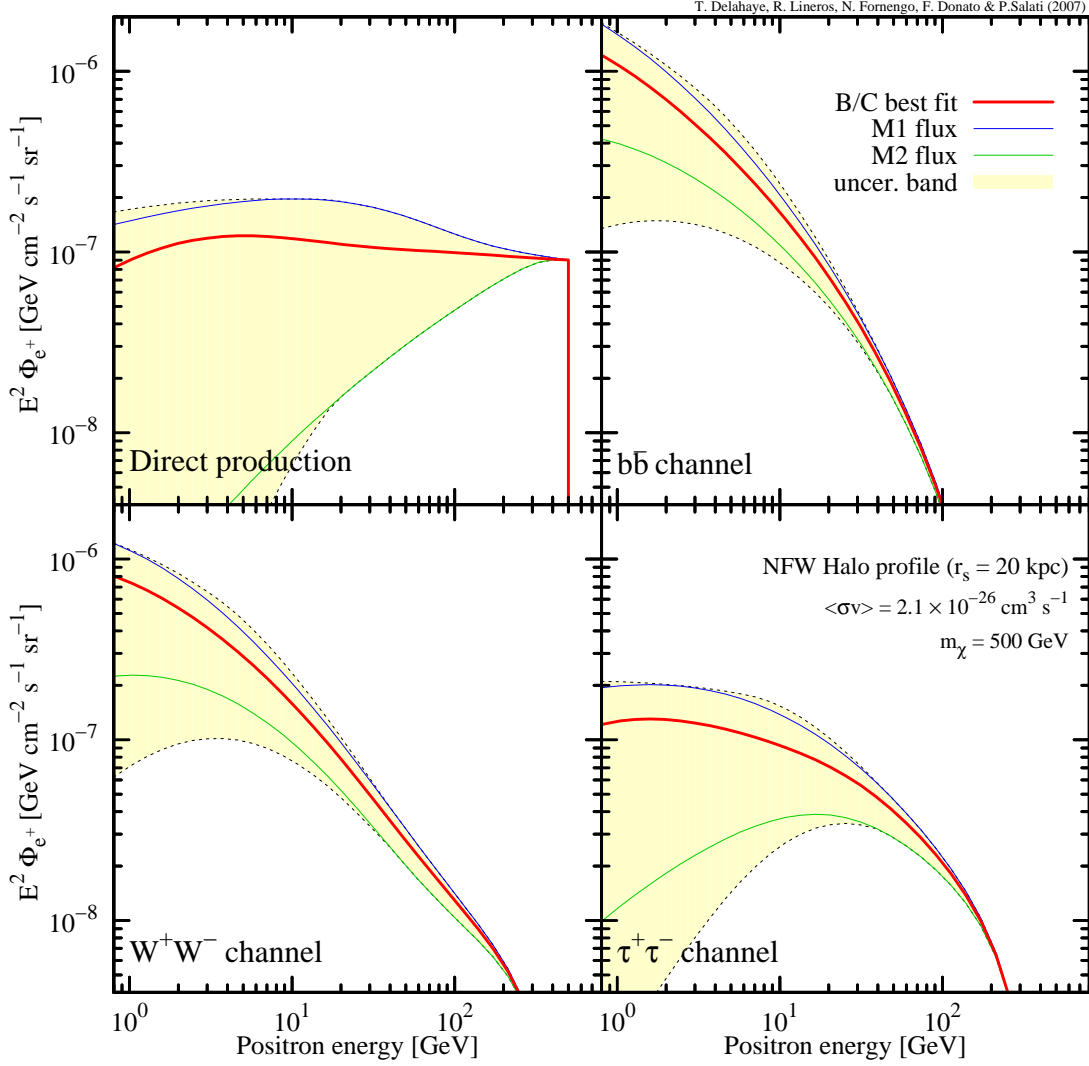


FIG. 8: Same plot as in Fig. 7 but with a DM particle mass of 500 GeV.

are detected at an energy  $E \sim E_S$ , they tend to have been produced not too far from the Earth, hence a lesser dependence to the propagation uncertainties. The astrophysical configuration M2 – see Tab. III – provides the minimal positron flux. It corresponds to the lower boundaries of the yellow uncertainty bands of Fig. 7. The M1 configuration maximizes the flux at high energies. For direct production and to a lesser extent for the  $\tau^+\tau^-$  channel, that configuration does not reproduce the upper envelope of the uncertainty band in the low energy tail of the flux. As discussed in Sec. III, the response of  $\Phi_{e^+}$  to the propagation parameters depends on the detected energy  $E$  in such a way that the maximal value

cannot be reached for a single astrophysical configuration. Finally, taking as a reference the median flux, the uncertainty bands extend more towards small values of the flux. In all channels, the maximal flux is typically a factor of  $\sim 1.5$ –2 times larger than the median prediction. The minimal flux features larger deviations with a factor of 5 for the  $b\bar{b}$  channel at  $E = 1$  GeV, of 10 for  $W^+W^-$  and of 30 for  $\tau^+\tau^-$ .

Fig. 8 is similar to Fig. 7 but with a heavier DM species of 500 GeV instead of 100 GeV. Since the mass  $m_\chi$  is larger, so is on average the injected energy  $E_S$ . Notice that at fixed positron energy  $E$  at the Earth, the radius  $\lambda_D$  of the positron sphere increases with  $E_S$ . We there-

fore anticipate that the propagated fluxes are affected by larger uncertainties for heavy DM particles. Again, the maximal flux does not exceed twice the median flux, while the minimal configurations are significantly depressed. At the reference energy  $E = 1$  GeV, reductions by a factor of 10 between the median and minimal predictions are obtained for the  $b\bar{b}$  channel and amount to a factor of 20 in the  $W^+W^-$  case. They reach up to 2 orders of magnitude for the direct positron production. In this large DM mass regime, the astrophysical configuration M2 does not reproduce by far the lower bound of the uncertainty band as it did for the 100 GeV case. The message is therefore twofold.

- (i) Once the positron spectrum at the source is chosen – and the corresponding branching ratios have been defined – the correct determination of the uncertainty which affects the flux at the Earth requires a full scan of the propagation parameter space for each energy  $E$ . The use of representative astrophysical configurations such as M1 and M2 would not provide the correct uncertainty over the entire range of positron energy  $E$ .
- (ii) However, specific predictions have to be performed for a given model of DM particle and a fixed set of astrophysical parameters. This is why fits to the experimental data should be performed for each propagation configuration over the entire range of the measured positron energies  $E$ . The best fit should correspond to a unique set of astrophysical parameters. This procedure is the only way to reproduce properly the correct and specific spectral shape of the flux.

The effect induced by different DM profiles is presented in Fig. 9, where the positron fluxes for the  $b\bar{b}$  and  $W^+W^-$  channels are reproduced for the DM distributions of Tab. I. The mass of the DM particle is fixed at  $m_\chi = 100$  GeV. Notice how steeper profiles entail larger uncertainties, especially for the upper bound. This is mostly due to the fact that for large values of  $L$  – for which larger fluxes are obtained – the positron flux is more sensitive to the central region of the Galaxy, where singular profiles like the NFW and Moore distributions have larger densities and therefore induce larger annihilation rates. On the contrary, the lower envelope of the uncertainty band is not affected by the variation of the halo profile. In this case, with typically small heights  $L$ , positrons reach the solar system from closer regions, where the three halo distributions are very similar and do not allow to probe the central part of the Milky Way.

Fig. 10 depicts the information on the positron flux uncertainty from a different perspective. The flux  $\Phi_{e^+}$  and

its uncertainty band are now featured for fixed values of the detected energy  $E$  whereas the DM particle mass is now varied. The flux  $\Phi_{e^+}$  is actually rescaled by the product  $E^2 m_\chi^2 \Phi_{e^+}$  for visual convenience. Each band corresponds to a specific detected energy  $E$  and consequently starts at  $m_\chi = E$ . In the case of the  $W^+W^-$  channel, the bands start at  $m_\chi = m_W$  because this channel is closed for DM masses below that threshold. The behavior of these bands can be understood from Fig. 6, where the halo function  $\tilde{I}$  is plotted for the same detected energies, as a function of the injection energy  $E_S$ . In the case of direct positron production, there is a simple link between the two figures, because the source spectrum in this case is just a line at  $E_S = m_\chi$ . For the other channels the situation is more involved since we have a continuous injection spectrum with specific features as discussed above. The main information which can be withdrawn from Fig. 10 is that at fixed detection energy, the larger the DM mass, the larger the uncertainty. Let us take for instance a detection energy of  $E = 3$  GeV. For direct production, where  $E_S = m_\chi$ , increasing the DM mass translates into a larger radius  $\lambda_D$  of the positron sphere. As a consequence, the uncertainty band enlarges for increasing masses. This occurs for all the annihilation channels, but is less pronounced for soft spectra as in the  $b\bar{b}$  case. Similar conclusions hold for all the other values of  $E$ .

Comparison with available data is presented in Fig. 11, 12 and 13. In Fig. 11, the positron fraction

$$\frac{e^+}{e^+ + e^-} \equiv \frac{\Phi_{e^+}^{\text{TOT}}}{\Phi_{e^-} + \Phi_{e^+}^{\text{TOT}}} \quad (32)$$

is plotted as a function of the positron energy  $E$ . The total positron flux  $\Phi_{e^+}^{\text{TOT}}$  at the Earth encompasses the annihilation signal and a background component for which we use the results of Ref. [1] as parameterized in Ref. [8] – see the thin solid [brown] lines. The electron flux is denoted by  $\Phi_{e^-}$ . The mass of the DM particle is 100 GeV and a NFW profile has been assumed. The data from HEAT [2], AMS [4, 5], CAPRICE [6] and MASS [7] are indications of a possible excess of the positron fraction for energies above 10 GeV. Those measurements may be compared to the thick solid [red] line that corresponds to the MED configuration. In order to get a reasonable agreement between our results and the observations, the annihilation signal has been boosted by an energy-independent factor ranging from 10 to 50 as indicated in each panel. At the same time, the positron background – for which we do not have an error estimate yet – has been shifted upwards from its reference value of Ref. [8] by a small amount of 10%. As is clear in the upper left panel, the case of direct production offers a very good agreement with the potential HEAT excess. Notice how

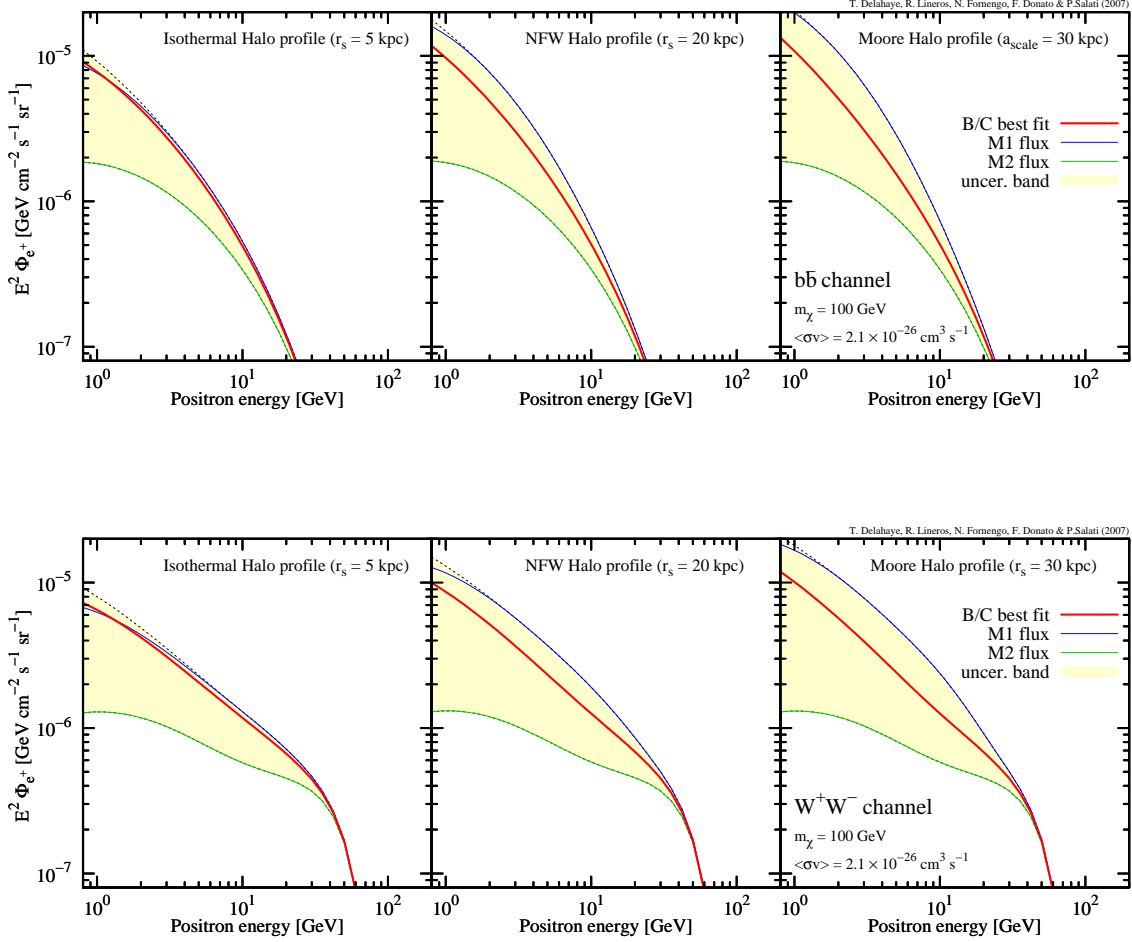


FIG. 9: Positron flux  $E^2\Phi_{e^+}$  versus the positron energy  $E$ , for a DM particle mass of 100 GeV and for different halo density profiles : cored isothermal sphere [21] (left panels), NFW [22] (central panels) and Moore [23] (right panels) – see Tab. I. The upper and lower rows correspond respectively to a  $b\bar{b}$  and  $W^+W^-$  annihilation channel. In each panel, the thick solid [red] curve refers to the best-fit choice (MED) of the astrophysical parameters. The upper [blue] and lower [green] thin solid lines stand for the astrophysical configurations M1 and M2 of Tab. III. The colored [yellow] area indicates the total uncertainty band arising from positron propagation.

well all the data points lie within the uncertainty band. A boost factor of 10 is enough to obtain an excellent agreement between the measurements and the median flux. A smaller value would be required for a flux at the upper envelope of the uncertainty band. The  $W^+W^-$  and  $\tau^+\tau^-$  channels may also reproduce reasonably well the observations, especially once the uncertainty is taken into account, but they need larger boost factors of the order of 30 to 40. On the contrary, softer production channels, like the  $b\bar{b}$  case, are unable to match the features of the putative HEAT excess for this value of the DM particle mass. For all annihilation channels, the uncertainty bands get thinner at high energies for reasons explained above. They surprisingly tend to shrink also at

low energies, a regime where the positron horizon is the furthest and where the details of galactic propagation are expected to be the most important. Actually, the annihilation signal turns out to be completely swamped in the positron background. In particular, the signal from direct production stands up over the background only for energies larger than 5 GeV. The corresponding uncertainty on the positron fraction is at most of the order of 50% for energies between 10 and 20 GeV. In the other cases, the uncertainty bands are even thinner. Beware finally of the positron background which should also be affected by uncertainties due to secondary production processes and propagation. These uncertainties are not currently available and there is clearly a need to estimate them in order

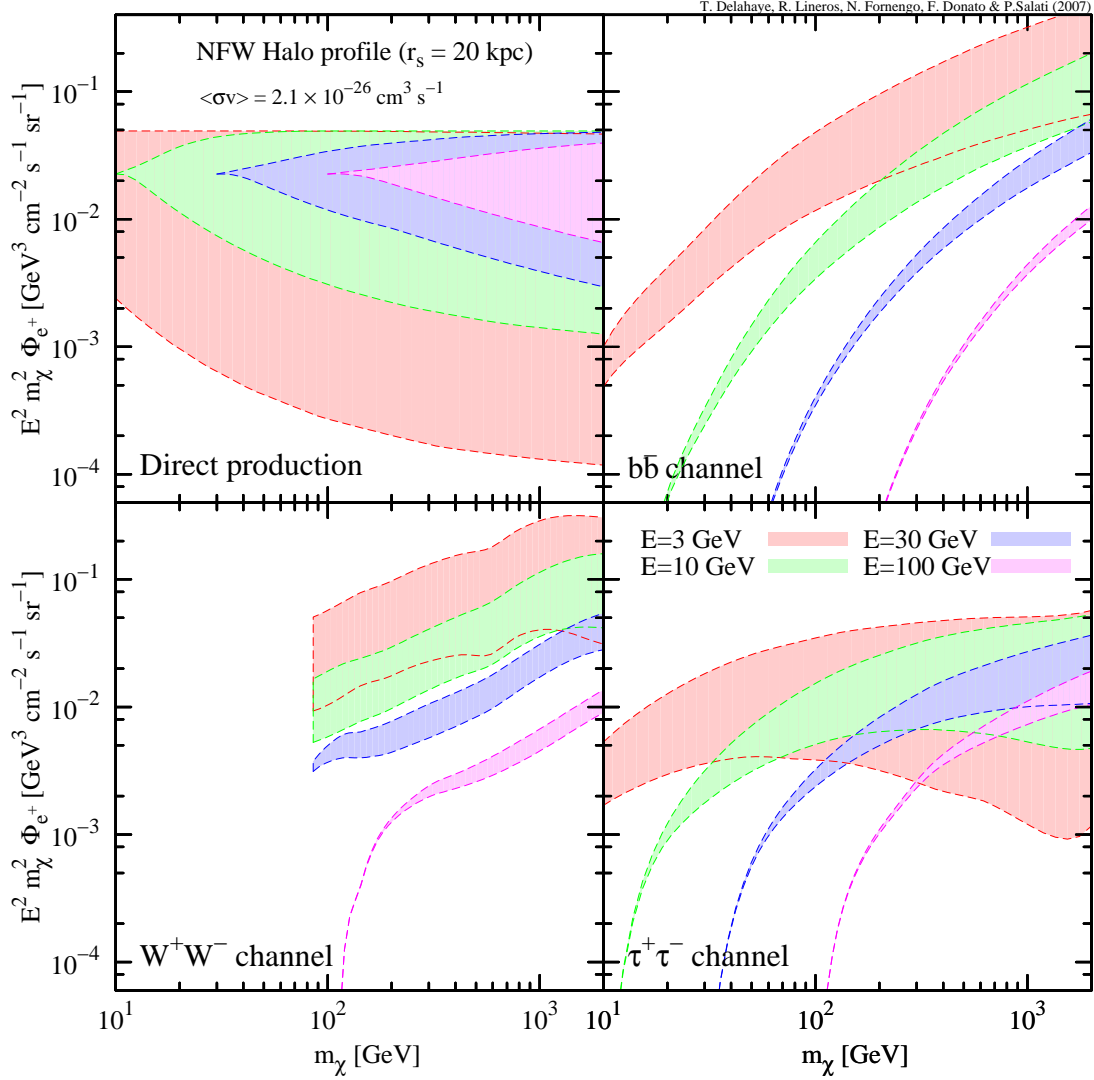


FIG. 10: For fixed values of the detected energy  $E$ , the uncertainty bands on the positron flux  $E^2 m_\chi^2 \Phi_{e^+}$  are shown as a function of the mass  $m_\chi$  of the DM particle. The energies considered in the figure are  $E = 3, 10, 30$  and  $100$  GeV. Each band refers to one of those values and starts at  $m_\chi = E$ .

to properly shape theoretical predictions and to perform better study of the current and forthcoming data. Such an investigation would involve a comprehensive analysis and is out of the scope of the present article.

Somehow different is the situation for larger masses of the DM candidate. Fig. 12 features the same information as Fig. 11, but now for  $m_\chi = 500$  GeV. In this case, all the annihilation channels manage to reproduce the experimental data, even the softest one  $b\bar{b}$ . For direct production, the positron fraction is very large at energies above 40 GeV, where no data are currently available.

This feature would be a very clear signature of DM annihilating directly into  $e^+e^-$  pairs, with strong implications also on the nature of the DM candidate. For instance, bosonic dark matter would be strongly preferred, since Majorana fermionic DM, like the neutralino, possesses a very depressed cross section into light fermions because of helicity suppression in the non-relativistic regime. Astrophysical uncertainties on the signal in this case show up more clearly than for the case of a lighter DM species, but still they are not very large. The drawback of having a heavier relic is that now the boost factors required to

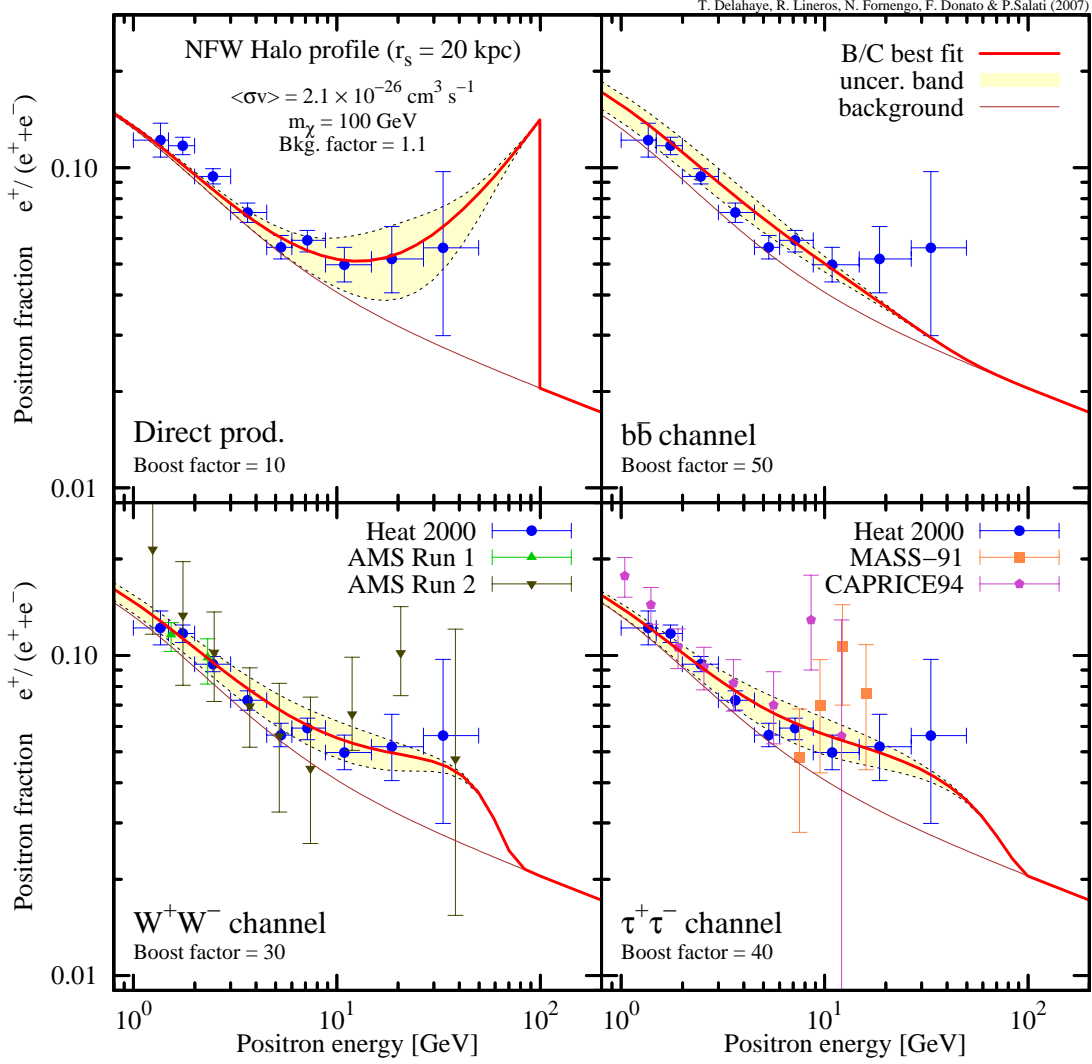


FIG. 11: Positron fraction  $e^+/(e^- + e^+)$  versus the positron detection energy  $E$ . Notations are as in Fig. 7. In each panel, the thin [brown] solid line stands for the background [1, 8] whereas the thick solid [red] curve refers to the total positron flux where the signal is calculated with the best-fit choice (MED) of the astrophysical parameters. Experimental data from HEAT [2], AMS [4, 5], CAPRICE [6] and MASS [7] are also plotted.

match the data are quite large. In Fig. 12 they range from 250 for the soft channel to 400 for the  $\tau^+\tau^-$  case. Such large boost factors appear to be disfavored, on the basis of the recent analysis of Refs. [10, 11].

In Fig. 13, the positron flux (not the fraction) is compared to the available experimental data for a 500 GeV DM particle and a NFW profile. The solid thin [brown] line features the positron background which we shifted upwards by 10% with respect to the reference value of Ref. [8]. The thick solid [red] line encompasses both

that background and the annihilation signal which we calculated with the best-fit choice (MED) of the astrophysical parameters. Both curves have been derived assuming solar modulation implemented through the force field approximation with a Fisk potential  $\phi_F$  of 500 MV. The dashed [red] line instead corresponds to the total positron interstellar flux without solar modulation. Notice that this curve is superimposed on the thick [red] line above  $\sim 10$  GeV, a regime where cosmic ray propagation is no longer affected by the solar wind. A reason-

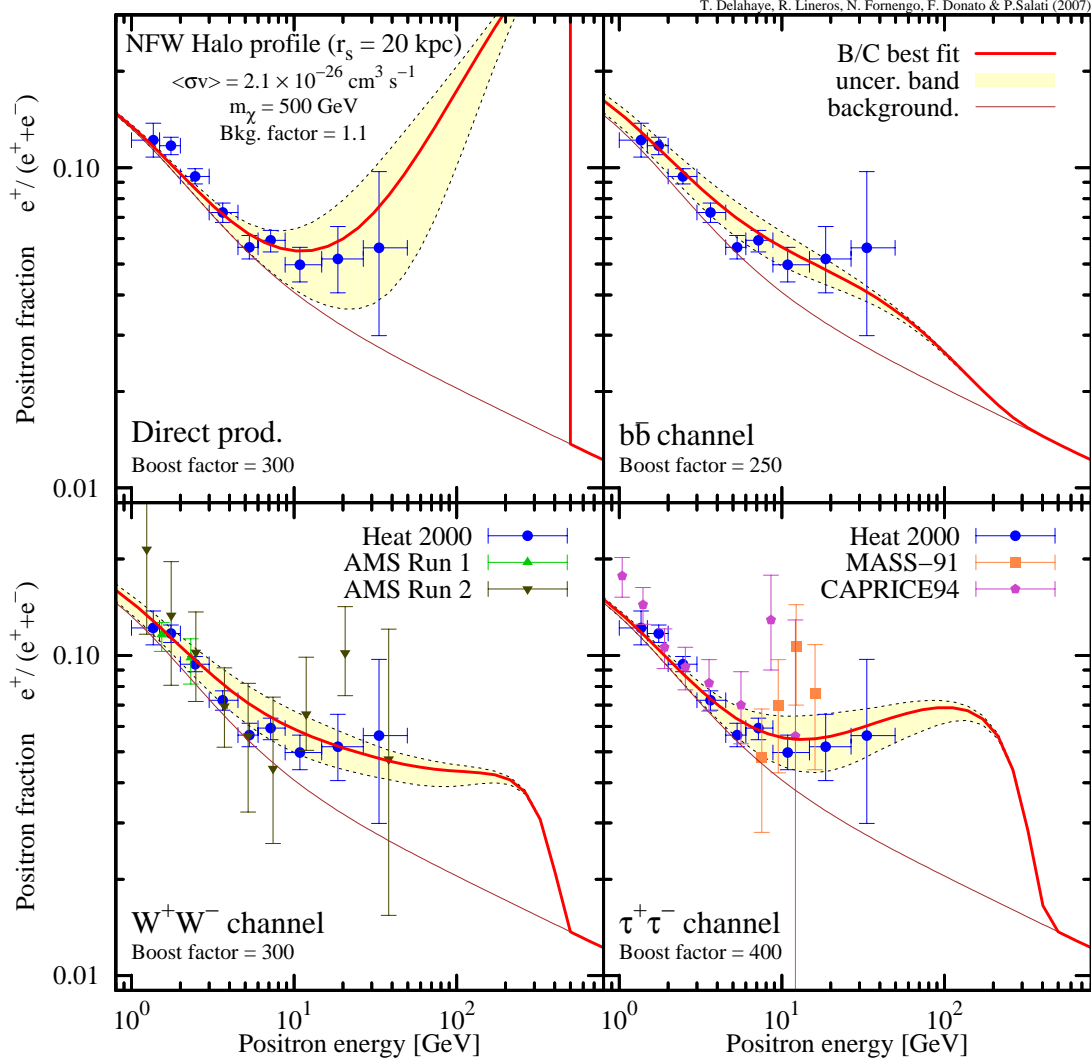


FIG. 12: Same plot as in Fig. 11 but with a mass of the DM particle of 500 GeV.

ably good agreement between the theoretical predictions and the data is obtained, especially once the theoretical uncertainties on the annihilation signal are taken into account. Notice that the spread of each uncertainty band is fairly limited as we already pointed out for the positron fraction. The reasons are the same.

Prospects for the future missions are shown in Fig. 14 and 15. In Fig. 14, a 100 GeV DM particle and a NFW halo profile have been assumed. The median [red] curve corresponds to the prediction for the best-fit MED choice of astrophysical parameters whereas the upper [blue] and lower [green] lines correspond respectively to the M1 and M2 propagation models – see Tab. III. Since we are deal-

ing with predictions which will eventually be compared to the measurements performed over an entire range of positron energies, we have to choose specific sets of propagation parameters as discussed above in this Section. The upper and lower curves therefore do not represent the maximal uncertainty at each energy – though they may do so in some limited energy range – but instead they are “true” predictions for a specific set of propagation parameters. Fig. 14 summarizes our estimate of the capabilities of the PAMELA detector [27] after 3 years of running. We only plotted statistical errors. We reach the remarkable conclusion that not only will PAMELA have the capability to disentangle the signal from the

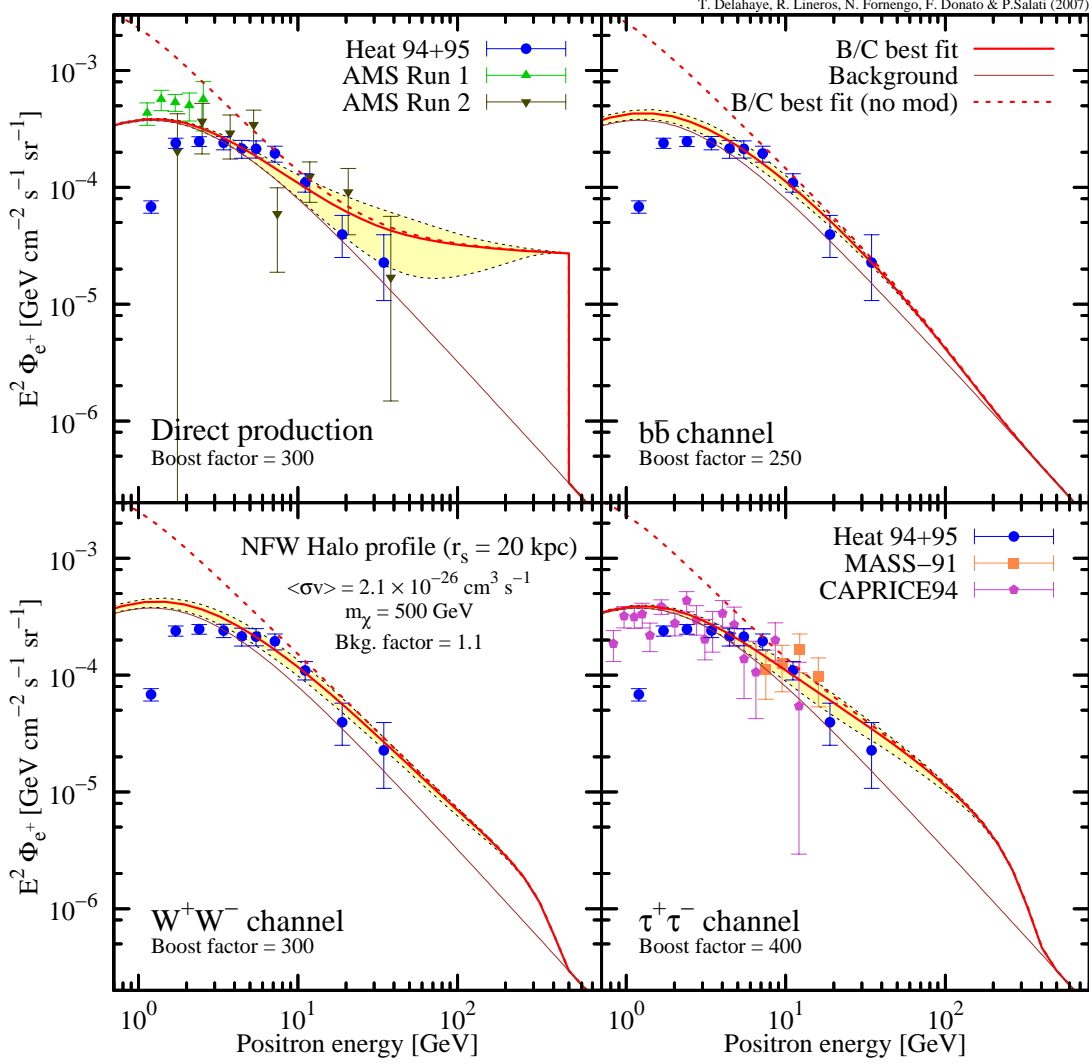


FIG. 13: Positron flux  $E^2\Phi_{e^+}$  (not fraction) versus the positron energy  $E$ , for a 500 GeV DM particle. Notations are the same as in Fig. 11. Experimental data from HEAT [2], AMS [4, 5], CAPRICE [6] and MASS [7] are plotted.

background, but also to distinguish among different astrophysical models, especially for hard spectra. Our conclusion still holds for the  $b\bar{b}$  soft spectrum for which the M1, MED and M2 curves of the upper right panel differ one from each other by more than a few standard deviations. PAMELA could be able to select among them, even when systematical errors are included.

In Fig. 15, the case of a 500 GeV DM particle is confronted with the sensitivity of AMS-02 for a 3-year flight. The possibility to disentangle the signal from the background is also clearly manifest here, even once the astrophysical uncertainties are included – provided though

that boost factors of the order of 200 to 400 are possible. But, unless direct production is the dominant channel, a clear distinction among the various astrophysical models will be very difficult because the M1 and M2 configurations are closer to the MED curve now than in the previous case of a lighter DM species. Comparison between Figs. 14 and 15 clearly exhibits that at least below the TeV scale, the effect of the mass  $m_\chi$  should not limit the capability of disentangling the annihilation signal from the background. More problematic is our potential to distinguish among different astrophysical models when the DM mass sizeably exceeds the 100 GeV scale.

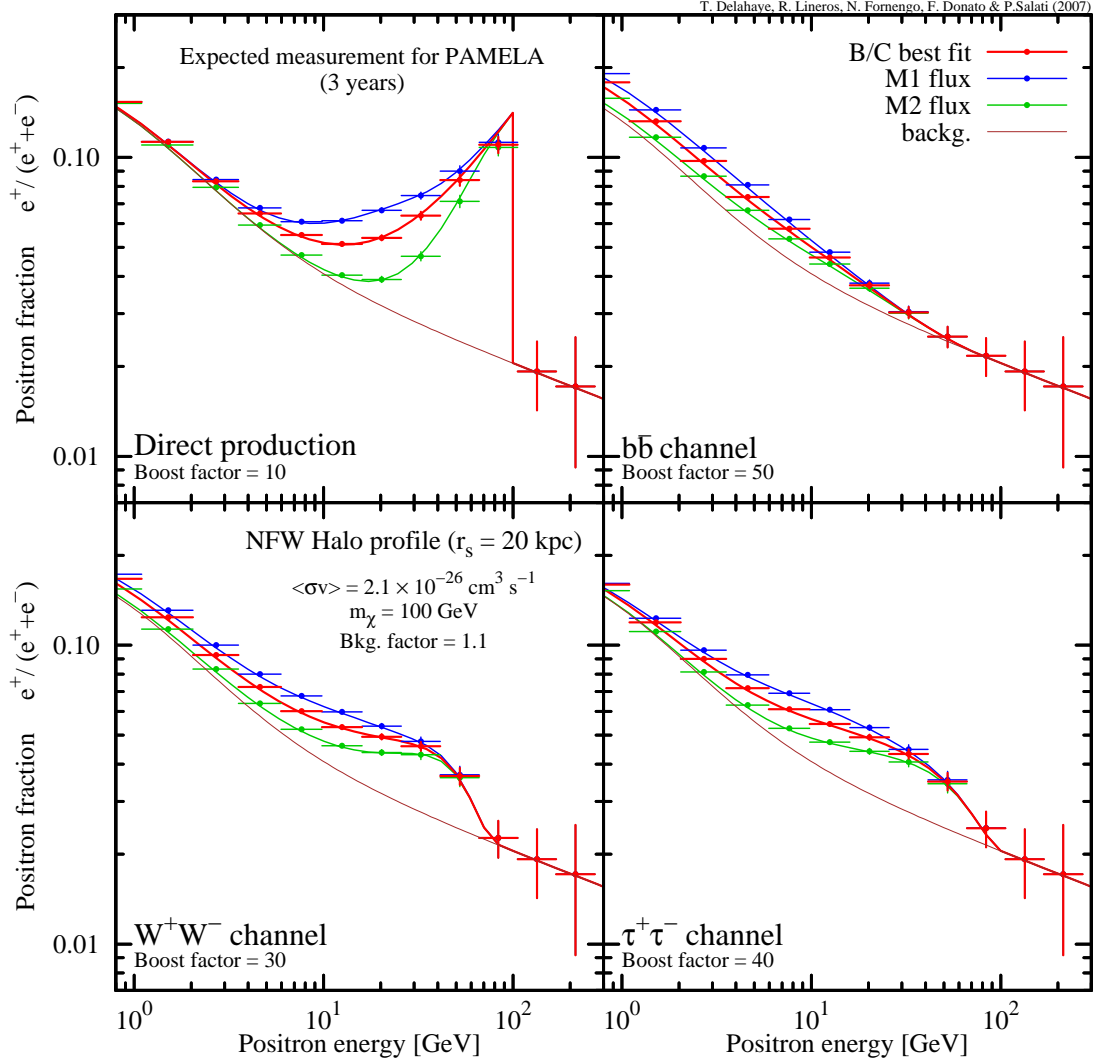


FIG. 14: Predictions for PAMELA for a 3-year mission. The positron fraction  $e^+/(e^- + e^+)$  and its statistical uncertainty are plotted against the positron energy  $E$  for a 100 GeV DM particle and a NFW profile. Notations are the same as in Fig. 11. The thick solid curves refer respectively to the total positron flux calculated with the M1 (upper [blue]), MED (median [red]) and M2 (lower [green]) sets of propagation parameters.

## V. CONCLUSIONS

We have analyzed the positron signal from DM annihilation in the galactic halo, focusing our attention to the determination of the astrophysical uncertainties on the positron flux due to the positron propagation inside the galactic medium.

Propagation of galactic cosmic rays has been treated in a two-zone model [12] and we have solved the diffusion equation for primary positrons both in the Green func-

tion formalism and with the Bessel expansion method. We find that the most efficient way of dealing with positron propagation is to adopt the Green function method for values of the diffusion length  $\lambda_D = \sqrt{4K_0\tau}$  smaller than  $\sim 3$  kpc, and to employ the Bessel function technique whenever  $\lambda_D$  becomes larger. In this way the radial boundaries of the diffusion region (which are neglected in the Green function approach) can be properly coped with by the Bessel expansion method.

The propagation uncertainties on the halo integral

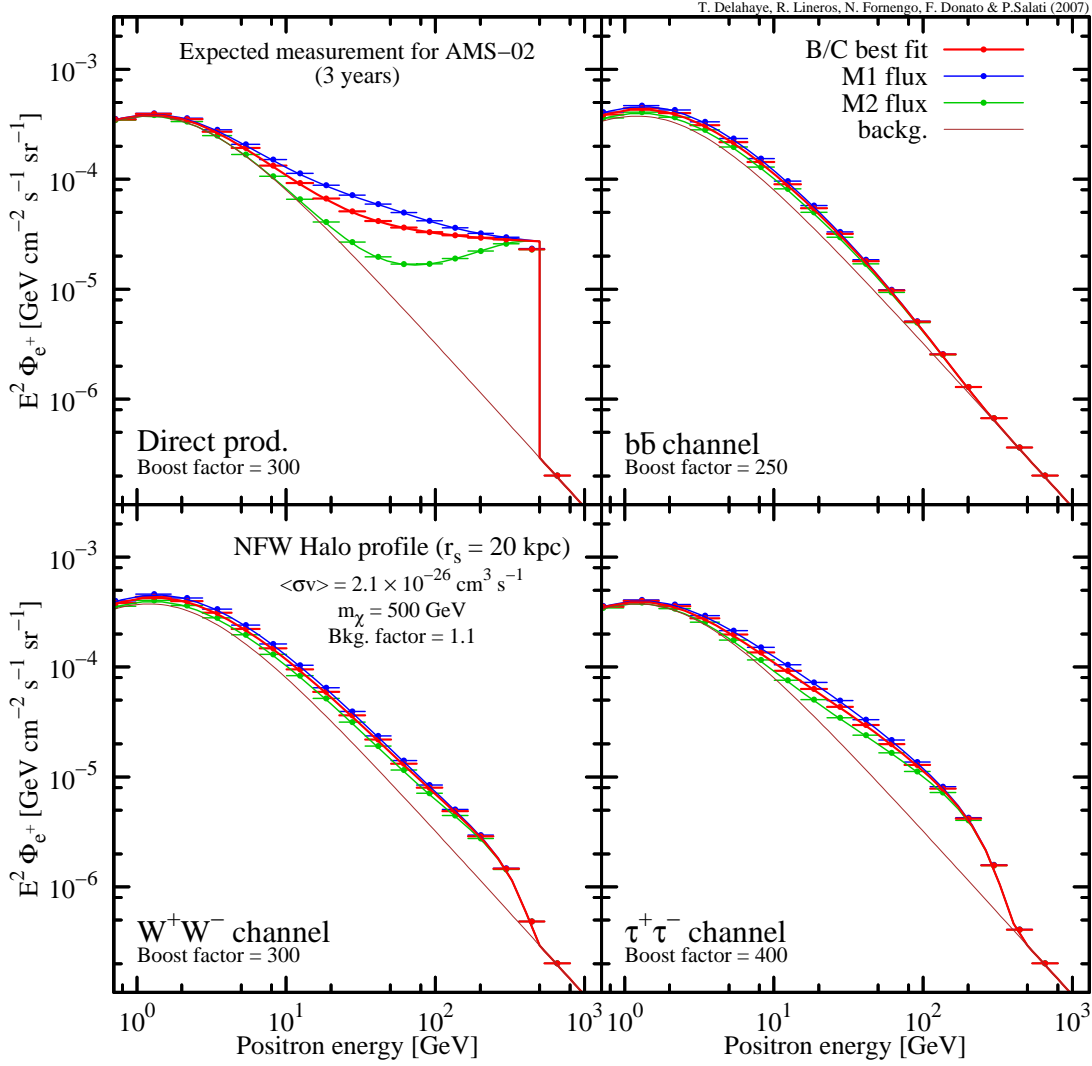


FIG. 15: Predictions for AMS-02 for a 3-year mission. The positron flux  $E^2\Phi_{e^+}$  and its statistical uncertainty are featured as a function of the positron energy  $E$  for a 500 GeV DM species and a NFW profile. Notations are the same as in Fig. 13. The thick solid curves refer respectively to the total positron flux calculated with the M1 (upper [blue]), MED (median [red]) and M2 (lower [green]) sets of propagation parameters.

have been calculated for the  $\sim 1,600$  different cosmic ray propagation models that have been found compatible [12] with the B/C measurements. These uncertainties are strongly dependent on the source and detection energies,  $E_S$  and  $E$ . As  $E_S$  gets close to  $E$ , we observe that each uncertainty domain shrinks. In that regime, the diffusion length  $\lambda_D$  is very small and the positron horizon probes only the solar neighborhood. In the opposite case, the uncertainty can be as large as one order of magnitude or even more. As positrons originate further from the

Earth, the details of galactic propagation become more important in the determination of the positron flux. On the contrary, high-energy positrons are produced locally and the halo integral  $\tilde{I}$  becomes unity whatever the astrophysical parameters.

Inspecting directly the positron fluxes, typically, for a 100 GeV DM particle annihilating into a  $b\bar{b}$  pair, uncertainties due to propagation on the positron flux are one order of magnitude at 1 GeV and a factor of two at 10 GeV and above. We find an increasing uncertainty for

harder source spectra, heavier DM, steeper profiles.

The comparison with current data shows that the possible HEAT excess is reproduced for DM annihilating mostly into gauge bosons or directly into a positron–electron pair, and the agreement is not limited by the astrophysical uncertainties. A boost factor of 10 is enough to obtain an excellent agreement between the measurements and the median flux, for a 100 GeV DM particle. A smaller value would be required for a flux at the upper envelope of the uncertainty band.

We have finally drawn prospects for two interesting 3–year flight space missions, like PAMELA, already in operation, and the future AMS-02. We reach the remarkable conclusion that not only will PAMELA have the capability to disentangle the signal from the background, but it will also distinguish among different astrophysical models, especially for hard spectra. For AMS-02 the possibility to disentangle the signal from the background is also clearly manifest. We also wish to remind that improved experimental results on cosmic ray nuclei, especially on the B/C ratio, will be instrumental to improve the determination of the parameters of the propagation models, and will therefore lead to sharper theoretical predictions. This in turn will lead to a more refined comparison with the experimental data on the positron flux. Moreover, a

good determination of the unstable/stable nuclei abundances like the  $^{10}\text{Be}/^9\text{Be}$  ratio could shed some light on the local environment, which is certainly mostly relevant to the positrons.

In the present paper we have thus presented the methods and the practical tools to evaluate the primary positron fluxes in detailed propagation models. We have provided careful estimations of the underlying uncertainties and shown the extraordinary potentials of already running, or near to come, space detectors.

### Acknowledgments

R.L., F.D. and N.F gratefully acknowledge financial support provided by Research Grants of the Italian Ministero dell’Istruzione, dell’Università e della Ricerca (MIUR), of the Università di Torino and of the Istituto Nazionale di Fisica Nucleare (INFN) within the *Astroparticle Physics Project*. R.L. also acknowledges the Comisión Nacional de Investigación Científica y Tecnológica (CONICYT) of Chile. T.D. acknowledges financial support from the French École Polytechnique and P.S. is grateful to the French Programme National de Cosmologie.

- 
- [1] I. V. Moskalenko and A. W. Strong, *Astrophys. J.* **493**, 694 (1998), astro-ph/9710124.
  - [2] S. W. Barwick et al. (HEAT), *Astrophys. J.* **482**, L191 (1997), astro-ph/9703192.
  - [3] S. Ahlen et al., *Nucl. Instrum. Meth. A* **350**, 351 (1994).
  - [4] J. Alcaraz et al. (AMS), *Phys. Lett.* **B484**, 10 (2000).
  - [5] M. Aguilar et al. (AMS-01), *Phys. Lett.* **B646**, 145 (2007), astro-ph/0703154.
  - [6] M. Boezio, P. Carlson, T. Francke, N. Weber, M. Suffert, M. Hof, W. Menn, M. Simon, S. A. Stephens, R. Bellotti, et al., *Astrophys. J.* **532**, 653 (2000).
  - [7] C. Grimani, S. A. Stephens, F. S. Cafagna, G. Basini, R. Bellotti, M. T. Brunetti, M. Circella, A. Codino, C. De Marzo, M. P. De Pascale, et al., *Astronomy & Astrophysics* **392**, 287 (2002).
  - [8] E. A. Baltz and J. Edsjo, *Phys. Rev.* **D59**, 023511 (1999), astro-ph/9808243.
  - [9] D. Hooper and J. Silk, *Phys. Rev.* **D71**, 083503 (2005), hep-ph/0409104.
  - [10] J. Lavalle, J. Pochon, P. Salati, and R. Taillet, *Astronomy & Astrophysics* **462**, 827 (2007), astro-ph/0603796.
  - [11] J. Lavalle, Q. Yuan, D. Maurin, and X. J. Bi (2007), arXiv:0709.3634 [astro-ph].
  - [12] D. Maurin, F. Donato, R. Taillet, and P. Salati, *Astrophys. J.* **555**, 585 (2001).
  - [13] H.-C. Cheng, K. T. Matchev, and M. Schmaltz, *Phys. Rev.* **D66**, 036005 (2002), hep-ph/0204342.
  - [14] G. Servant and T. M. P. Tait, *Nucl. Phys.* **B650**, 391 (2003), hep-ph/0206071.
  - [15] T. Appelquist, H.-C. Cheng, and B. A. Dobrescu, *Phys. Rev.* **D64**, 035002 (2001), hep-ph/0012100.
  - [16] A. Bottino, N. Fornengo, and S. Scopel, *Phys. Rev.* **D67**, 063519 (2003), hep-ph/0212379.
  - [17] A. Bottino, F. Donato, N. Fornengo, and S. Scopel, *Phys. Rev.* **D68**, 043506 (2003), hep-ph/0304080.
  - [18] G. Belanger, F. Boudjema, A. Pukhov, and S. Rosier-Lees, *Phys. Rev.* **D68** (2003), hep-ph/0310037.
  - [19] D. Hooper and T. Plehn, *Phys. Lett.* **B562**, 18 (2003), hep-ph/0212226.
  - [20] T. Sjostrand et al., *Comput. Phys. Commun.* **135**, 238 (2001), hep-ph/0010017.
  - [21] J. N. Bahcall and R. M. Soneira, *Astrophys. J. Suppl.* **44**, 73 (1980).
  - [22] J. F. Navarro, C. S. Frenk, and S. D. M. White, *Astrophys. J.* **490**, 493 (1997), astro-ph/9611107.
  - [23] J. Diemand, B. Moore, and J. Stadel, *Mon. Not. Roy. Astron. Soc.* **353**, 624 (2004), astro-ph/0402267.
  - [24] F. Donato, N. Fornengo, D. Maurin, P. Salati, and R. Taillet, *Phys. Rev.* **D69**, 063501 (2004).
  - [25] F. Donato et al., *Astrophys. J.* **563**, 172 (2001).
  - [26] D. Maurin and R. Taillet, *Astron. Astrophys.* **404**, 949 (2003), astro-ph/0212113.
  - [27] M. Boezio et al., *Nucl. Phys. Proc. Suppl.* **134**, 39 (2004).